MODEL-BASED OPTIMIZATION OF MICROSCALE PARTS PRINTED WITH PROJECTION-BASED CONTINUOUS VAT PHOTOPOLYMERIZATION

A THESIS SUBMITTED TO

THE GRADUATE SCHOOL OF ENGINEERING AND SCIENCE

OF BILKENT UNIVERSITY

IN PARTIAL FULFILLMENT OF THE REQUIREMENTS FOR

THE DEGREE OF

MASTER OF SCIENCE

IN

MECHANICAL ENGINEERING

By

Ege Güven

August 2022

MODEL-BASED OPTIMIZATION OF MICROSCALE PARTS PRINTED WITH PROJECTION-BASED CONTINUOUS VAT PHOTOPOLYMERIZATION
By Ege Güven
August 2022

We certify that we have read this thesis and that in our opinion it is fully adequate, in scope and in quality, as a thesis for the degree of Master of Science.

Melih Çakmakçı(Advisor)

Yiğit Karpat(Co-Advisor)

Emine Yegan Erdem

Sezer Özerinç

Approved for the Graduate School of Engineering and Science:

Orhan Arıkan
Director of the Graduate School

ABSTRACT

MODEL-BASED OPTIMIZATION OF MICROSCALE PARTS PRINTED WITH PROJECTION-BASED CONTINUOUS VAT PHOTOPOLYMERIZATION

Ege Güven
M.S. in Mechanical Engineering
Advisor: Melih Çakmakçı, Yiğit Karpat
August 2022

Micro-scale additive manufacturing has seen significant growth over the past years, where improving the accuracy of complex micro-scale geometries is seen as an important challenge. Using grayscale images rather than black and white images during production is an effective method to improve the fabrication quality. This thesis presents a model-based optimization method for improving the dimensional accuracy of parts using voxel-based grayscale dynamic optimization during continuous 3D printing. A detailed solidification model has been developed and used to estimate the curing dynamics of the resin used in 3D printing. The irradiance of the light beam projected for each pixel influences a larger volume on the resin than the targeted voxel. The proposed model-based method optimizes the images considering the light distribution from all closely related pixels to maintain the accuracy of the micro part. The results of this method have been applied to the printing of complex 3D parts to show that optimized grayscale images improve the areas with overcuring significantly. It is shown that the number of overcured voxels was reduced by 24.7% compared to the original images. Actual printing results from the experimental setup confirm the improvements in the accuracy and precision of the printing method. The optimization method has been further improved by allowing variable printing speed during production and optimizing the speed profile of the print alongside grayscaling. This approach allows for printing of certain geometries that would otherwise be challenging to produce accurately. Computational limitations of performing speed and grayscale optimization simultaneously has been overcome by utilizing the symmetry of certain special cases to reduce optimization variables.

Keywords: process planning, vat photopolymerization, modeling, dynamic optimization, variable printing speed.

ÖZET

PROJEKSİYON TEMELLİ DEVAMLI KÜVET FOTOPOLİMERİZASYONU İLE YAZDIRILMIŞ MİKRO ÖLÇEKLİ PARÇALARIN MODEL BAZLI OPTİMİZASYONU

Ege Güven
Makine Mühendisliği, Yüksek Lisans
Tez Danışmanı: Melih Çakmakçı, Yiğit Karpat
Ağustos 2022

Mikro ölçekli eklemeli üretim, karmaşık mikro ölçekli geometrilerin doğruluğunun arttırılmasının önemli bir sorun olarak görüldüğü son yıllarda ciddi gelişme kaydetmiştir. Üretimde siyah beyaz yerine gri tonlamalı resimlerin kullanılması üretim kalitesini arttırmaktadır. Bu tez, devamlı 3D yazdırmada voksel temelli gri tonlamalı dinamik optimizasyon kullanarak parçaların boyutsal doğruluğunu geliştirmek için kullanılabilecek model bazlı bir optimizasyon yöntemi sunar. Detaylı bir katılaşma modeli geliştirilmiş ve 3D yazdırmada kullanılan reçinenin kürleme dinamiklerini tahmin etmede kullanılmıştır. Her piksele yansıtılan ışık huzmesinin dağılımı reçinede hedeflenen vokselden daha büyük bir hacmi etkiler. Önerilen model bazlı yöntem mikro parçanın doğruluğunu korumak için resimleri, yakındaki tüm piksellerin ışık dağılımını da hesaba katarak optimize eder. Bu yöntemin sonuçları, gri tonlamalı resimlerin fazla kürlenen alanları geliştirdiğini göstermek için 3 boyutlu karmaşık bir parçanın yazdırılmasına uygulanmıştır. Orijinal resimlerle karşılaştırıldığında fazla kürlenen voksel sayısının %24.7 azaldığı gösterilmiştir. Deney düzeneğinde yazdırılan gerçek yazdırma sonuçları yazdırma yönteminin doğruluğu ve kesinliğinin arttığını doğrulamaktadır. Optimizasyon yöntemi gri tonlamanın yanı sıra üretim sırasında değişken yazdırma süresine izin vererek ve yazdırmanın hız profilini optimize ederek de geliştirilmiştir. Bu yaklaşım aksi takdirde doğru üretimi zor olacak belli geometrilerin de yazdırılmasını sağlar. Hız ve gri tonlama optimizasyonu gerçekleştirmenin hesaplama sınırları optimizasyon değişkenlerini azaltmak için belirli özel durumların simetrisini kullanarak aşılmıştır.

Anahtar sözcükler: Süreç planlaması, küvet fotopolimerizasyonu, modelleme, dinamik optimizayon, değişken yazdırma hızı.

Acknowledgement

I would like to thank my advisors, Asst. Prof. Melih Çakmakçı and Assoc. Prof. Yiğit Karpat, for their guidance, supervision and support. I would like to express my gratitude to my friend and colleague Mr. Abdulrzak Masrani for his friendship and assistance throughout my studies. I am deeply grateful to my loving partner Nevgül Güven, thank you for all the love and support not only during my studies but every day. Last, but not least, I would like to express my sincere gratitude to my parents Akın and Deniz Güven, for their unwavering support and belief in me.

I acknowledge that I was supported by TUBITAK 2211 National Graduate Scholarship Program and that the equipment used in this research was partly sponsored by the Scientific and Technical Research Council of Turkey (TUBITAK), Project No: 113M172. [‘Development of a Multipurpose Micro Manufacturing System using Modular and Iterative Learning Control Algorithms‘]

Contents

List of Figures

List of Tables

Chapter 1

Introduction

Vat Photopolymerization (VPP) is a popular method for obtaining polymer-based parts due to its fast production speed, flexibility of the objects that can be produced, and high accuracy [1], [2]. VPP can be used on its own or along with various other additive manufacturing processes to produce complex parts [3]. Additive manufacturing systems that use the VPP approach typically consist of a vertical positioning system, a light source, and a container. The part is built gradually using the vertical positioning system to lower the platform as the polymer resin is cured at the locations where the ultraviolet light is projected. To achieve superior dimensional precision, it is essential to have precise control of the motion of the positioning system and the intensity of the light source, along with an understanding of the material properties of polymer resin. Utilization of a high pixel density DMD chip allows building of micro-scale parts with high accuracy and relatively low-cost [4].

1.1 Vat Photopolymerization Workflow

In order to prepare the desired part for production, its computer-generated solid model is sliced vertically into layers. These layers are recorded as digital black and white images representing the dimensional features of the part at different heights. These images are then projected on the resin surface during the VPP process so that the part is produced layer-by-layer.

1.1.1 Light Source

In general, there are two ways to project light onto the resin: vector scanning and projection. When using the vector scanning approach, each non-black pixel (point) on the layer image is scanned using a focused light source such as a laser. Once every point on a layer is scanned, the platform is moved vertically, and the curing of the next layer starts [5]. With the projection-based light source approach, an entire layer is cured at once with the help of a light projector or an LCD screen using the layer images [6].

1.1.2 Print Direction

A vat photopolymerization system can be configured in two ways based on the direction of the light projected on the resin. In the top-down configuration, the light projector is placed above the resin vat, and the platform starts from the surface of the resin and descends into the vat. For the bottom-up configuration, the projector screen is set up below the vat, and the platform starts from one layer thickness above the transparent bottom of the vat.

1.1.3 Platform Motion

The vertical motion of the platform may be advanced in two ways: layer-by-layer and continuous. With layer-by-layer printing, the platform is moved when the production of each layer is finished. In continuous printing, the platform moves continuously, and the projected images are changed in a timed or position-triggered fashion. Continuous printing produces a better surface finish since no layer marks are present. However, the platform's speed must be arranged carefully to avoid undercuring. In this paper a continuous top-down approach has been utilized.

1.2 Literature Review

In recent years, significant advances in vat photopolymerization have improved the dimensional accuracy of the parts produced. One of the most significant approaches is the utilization of grayscale masks instead of binary, i.e., black and white, masks. In earlier examples in the literature, the grayscale modifications were done manually, graying certain parts of the layer images. For example, in Lee et al. [7], Park et al. [8] and Mostafa et al. [9], researchers improved the resolution of their parts by grayscaling the images they project. These methods are primarily based on trial and error, and their application may not be feasible for improving parts with more complex geometries. More recently, Zhou et al. used linear programming optimization to reduce boundary errors and achieve sub-pixel resolution [10], [11]. Their method focuses primarily on the boundaries of the individual layers and employs a simpler curing model for their study. While the proposed formulation improves the horizontal (XY) resolution significantly, it disregards the errors in the z-direction and is prone to over-curing if overhanging structures are introduced. Pritchard et al. [12] and Bonada et al. [13] used grayscale images to reduce *cure-through* in continuous printing. Their correction model only considers the overcuring in the z-direction and does not account for the horizontal irradiation distribution and its effect on curing. Wang et al. mapped the power density distribution of their projector and used grayscaling to counteract the effects of uneven distribution in large objects [14]. Lichade et al. used grayscale images with continuous printing to improve the surface quality and reduce the porosity of fabricated parts [15]. You et al. utilized neural network-based machine learning to produce grayscale masks to counteract the effects of light scattering [16]. Dithering effect has been shown to be a viable alternative for achieving grayscale equivalent layer images in monochromatic systems [8, 17] Xu et al. incorporated an additional auxiliary platform to their VPP system to achieve higher control on the z-resolution while building microfluidic devices [18]. Haiyang et al. used machine learning to determine the ideal printing speed for a VPP system [19].

Photobleaching is the decomposition of the photoinitiator inside the resin as it cures [20]. Emami et al. demonstrated the photobleaching effect in photocurable resins and developed a multiphysics model to address its effects on printed parts [21, 22]. They have also modeled the propagation and attenuation of light within the resin to increase the dimensional accuracy of Cured VPP parts [23]. Ray tracing was used to model the irradiation inside the resin by Limaye et al. to be used as part of a VPP layer cure model [24]. A technique for analytically determining the Jacobs working curve [5] for a photocurable material has been developed by Li et al. [25]. They used the solid absorbance, liquid absorbance, and gelation time of the polymer resin to produce an analytical *Jacobs working curve* which agrees with the experimental results with less time and material waste. This robust method for determining the properties of a resin has been used by many researchers. After the properties of the material and the light source are characterized, the results can be utilized as a solidification model, predicting the part dimensions given production parameters. Westbeek et al. developed a multi-physical modeling framework to predict the defects a printed part will have without the need for a test print [26]. In [27], authors developed a workflow for fabricating micro-needles intended for transdermal drug delivery after parameter optimization based on the design of experiments. Moreover, the developed solidification model can improve the process by using online or offline optimizations. Li et al. developed a tunable pre-curing approach to improve fidelity and efficiency in [28] by keeping the resin at a gelled state during printing. Wicker et al. designed a multiple vat VPP system for building multi-material parts with a wide variety of materials, resulting in various part functionalities [29]. Tureyen et al. developed an iterative learning controller for improving accuracy in micro-scale vat photopolymerization systems [30] with the use of a one-dimensional solidification model. Pan et al. developed a method that utilizes the capillary properties of the resin to reduce the stair-step effect between layers caused by layer-by-layer printing and improve the surface finish [31]. However, this method requires a second round of light exposure after the part is removed from the resin, making the process more complex. Smith et al. developed a VPP method that allows layer-by-layer fabrication without a moving platform for microfluidic device production [32]. Danielak et al. designed a build plate for VPP systems to allow the part to attach to the build platform easier and more reliably [33].

With VPP it is possible to print with a wide variety of materials, depending on how the resin is formulated and what is mixed into it [34]. The research on incorporating various materials into the resin to manufacture parts with unique properties has also come a long way. VPP offers flexible and reliable means of manufacturing functionally graded materials [35]. A wide range of possible resin formulations makes VPP a prime candidate for 4D printing, in which the 3d printed object transforms into a predefined structure upon external stimuli [36, 37]. With 3d printing of parts with multiple different materials, unique properties and functions can be achieved [38, 39].

1.3 Motivation and Contribution of This Study

This thesis presents a model-based dimensional accuracy improvement method using a voxel-based grayscale dynamic optimization. In VPP systems, each pixel in the layer images represents the unit volume of the built part, called a *voxel*. During the production, the irradiance of the light beam projected for each pixel is not entirely confined to the targeted voxel, and it lights up a predictable region inside the resin, transferring energy for curing to a larger volume than the targeted voxel. Therefore, the images sent to the projector should be optimized considering the light distribution from all pixels to get a cured object as close as possible to the original CAD model. Although experimental validations for the method are presented using a top-down with continuous motion projection-based system primarily targeting micro-scale parts, the approach is generic enough to be extended to all VPP systems.

1.4 Thesis Structure

The outline for the remaining parts of this thesis is as follows. In Chapter 2, the experimental vat photopolymerization setup, polymer resin selection, and the print procedure are given. In Chapter 3, a mathematical model that predicts the solidification process is presented. Chapter 4 proposes the model-based projection optimization with dynamic programming. Chapter 5 describes the modifications and additions to the mathematical model and optimization algorithm to optimize variable print speed alongside the projection images. Lastly, Chapter 6 discusses the results and possible future work.

Chapter 2

Experimental Setup and Materials

2.1 Experimental Setup

The overall schematic of the rapid prototyping machine used in this study is given in Figure 2.1. The layer images are sent to the DLP projector in coordination with a precision positioning system that moves the platform using a workstation computer.

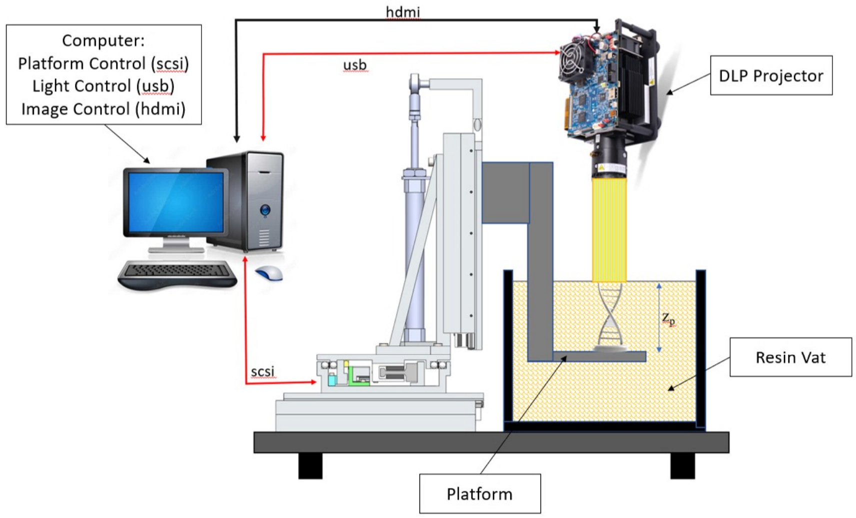

Figure 2.1: Photograph of the overall rapid prototyping system and its schematic. The Build chamber is enclosed in red glass to avoid curing of the resin from outside light sources.

The list of equipment and materials used to build and analyze a part is given in Table 2.1. Optimization is performed on a separate computer running a Ryzen 5 3600 processor with 64 GBs of DDR4 ram.

No:	Equipment / Material	Brand / Model
1	Positioning System and Controller	Aerotech A3200
2	Projector	Texas Instruments DLP4710EVM
3	Computer	Intel Xeon W3503 Workstation
4	Microscope	Keyence VHX-1000
5	High speed microscope	Keyence VW-9000
6	Scanning Electron Microscope	FEI Quanta 200 FEG ESEM

Table 2.1 Equipment and material list.

The pixel pitch of the DMD chip is $5.4\mu m$ and the projected pixels are $11.2\mu m$ squares. Further information on the light source can be found in the projector datasheet [40].

2.2 Polymer Resin

Absorption levels of various resins were examined using a Cary 100 spectrometer. The polymer resin used in all experiments is the *zSG Amber* by Uniz. After comparison with alternatives, zSG Amber has relatively high absorption near the visible blue light wavelength emitted by the projector's LED, between $444-465nm$ as shown in Figure 2.2.

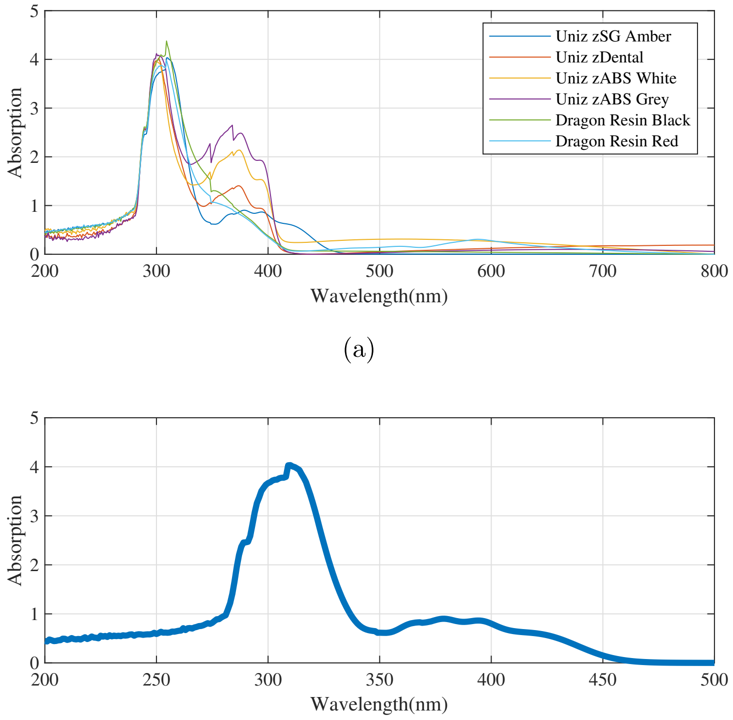

(a)

(b)

Figure 2.2: (a) $200-800nm$ spectroscopy results for all polymer resins considered. The small hill around $400nm$ allows for the curing of the resin in the visible light range. (b) $200-500nm$ spectroscopy results for the Uniz zSG Amber resin. This resin was chosen due to its superior absorption in the $444-465nm$ range, the emission range of the blue LED in the projector.

2.3 Print Process Outline

The process of building a part begins with drawing the part in CAD software. The part is then sliced into layer images. The optimization process modifies the layer images. The layer images are then turned into a video using editing software. The video is projected onto the resin surface while the platform is continuously lowered into the polymer resin vat. At the end of the video, the light from the projector is switched off, and the platform is raised above the resin. The built part is retrieved from the platform and is cleaned with isopropyl alcohol. Finally, the part is placed into a UV light bath for 5 minutes to be fully cured. The cured part is measured and photographed using the Keyence VHX-1000 microscope. A scanning electron microscope is used if higher accuracy measurements or better images are needed.

Chapter 3

Solidification Model

Mathematical models describing the underlying physical mechanisms of a process are developed as a first step to propose calculated improvements. For VPP systems, using mathematical equations to represent the layer-by-layer production of a part involves combining optical and chemical principles with platform motion dynamics.

3.1 Development of the Mathematical Model

In order to relate the projected image and the platform motion to the part dimensions as the model output, a coordinate system is defined as shown in Figure 3.1. Here, the resin surface is considered as the $z = 0$ level, and one of the corners of the projected image is taken as the origin with $x = 0$ and $y = 0$.

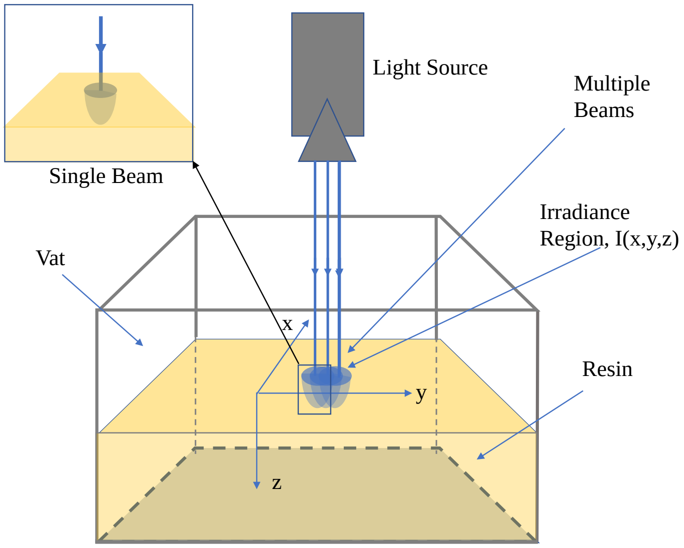

Figure 3.1: Irradiance of multiple light beams on a photo-polymeric resin surface where calculation by applying superposition of the irradiance of single beams is possible.

Understanding the behavior of the light beam as it penetrates the resin is crucial to estimating how the resin will cure when exposed to a layer image from the projector. A projected image can be considered as a collection of light beams entering the resin. For example, in Digital Light Processing (DLP) projectors, the layer image projected on the resin surface comprises pixel lights generated by individual micro-mirrors on the Digital Micro Device (DMD) chip [14]. A model that explains how a single pixel of light behaves in the resin can predict the behavior of a projected image composed of many light beams using the superposition principle.

The absorption of light inside a liquid can be modeled using the *Beer-Lambert Law*:

$$I(z) = I_0\, e^{-\mu z} \tag{3.1}$$

where $I(z)$ is the irradiance at z, I_0 is the irradiance on the resin surface, and μ is a penetration constant. As an alternative to the form presented in Eq.(3.1) a transmittance function, $T(z)$, can be defined as

$$T(z) = e^{-\mu z} = 10^{-cz} \tag{3.2}$$

where c is the absorption constant for the liquid.

The Beer-Lambert Law is presented as a one-dimensional relationship applied in the vertical (liquid depth) direction. However, many researchers have observed that the light distribution and absorption profile in the resin is not a beam shape with uniformly decreasing irradiance (such as [10], [11]), and it somewhat resembles a distorted cone shape, as shown in Figure 3.1. Therefore, the distribution of light on the resin surface and layers below should be included in the irradiance formulation for more accurate results. The effect of light distribution can be represented in irradiance calculations using a two-dimensional distribution function as shown in Eq.(3.3).

$$I_0(x, y) = a \cdot e^{-\left(\frac{(x-x_0)^2}{2\sigma_x^2} + \frac{(y-y_0)^2}{2\sigma_y^2}\right)} \tag{3.3}$$

The equation given in Eq.(3.3) is a typical Gaussian distribution function with two variables (x, y) with centering parameters (x_0, y_0) and distribution parameters σ_X and σ_Y. In addition, a constant, a, is also introduced to account for the grayscale value of a particular pixel in the layer images projected from the light source. By re-arranging Eq.(3.1) and Eq.(3.3), the irradiance from a single pixel of light entering the surface at (x_0, y_0) on a point with the coordinates (x, y, z) can be calculated as shown in Eq.(3.4)

$$I_{single}(x, y, z) = a \cdot e^{-\left(\frac{(x-x_0)^2}{2\sigma^2} + \frac{(y-y_0)^2}{2\sigma^2}\right)} \cdot 10^{-cz} \tag{3.4}$$

The constants $\sigma = \sigma_X = \sigma_Y$, and c determine the distribution of light in x and y directions respectively and are generally found with experiments. Understanding their effect on the general form of light absorption is necessary for identifying model constants. Analyzing Eq.(3.4) shows that increasing c reduces the amplitude as it increases the absorption, whereas increasing σ widens the boundaries as it increases the standard deviation of the Gaussian function. The light absorption distribution of multiple pixels can easily be modeled by superposing the single-pixel light distributions centered around each lit pixel, as shown in Figure 3.1. With the calculation of irradiance of multiple pixel light, a solidification model can be formulated to predict the production results of parts with various shapes.

Before VPP manufacturing, the part's solid model is sliced into k layers, and an image is produced for each layer. A layer is a digitized approximation of a part at a specific height. Assuming uniform thickness for each layer, as the number of layers increases (i.e., $K \to \infty$), this approximation of the part becomes more accurate. Each of these layer images is shown on the projector screen during manufacturing. In Figure 3.2, the slicing and layer preparation process of the simple part is shown. The target shape is a hollow square prism, which is first sliced and pixelated for production, and the voxel definitions are formed. When the layer images, which are composed of pixels, are assumed to represent the part's features with a specific thickness, this new unit volumetric area is defined as a voxel. The shape in Figure 3.2 is sliced in to l layers and represented with $l \times f \times h$ voxels. Each layer with $f \times h$ pixels is shown from the projector to produce the part.

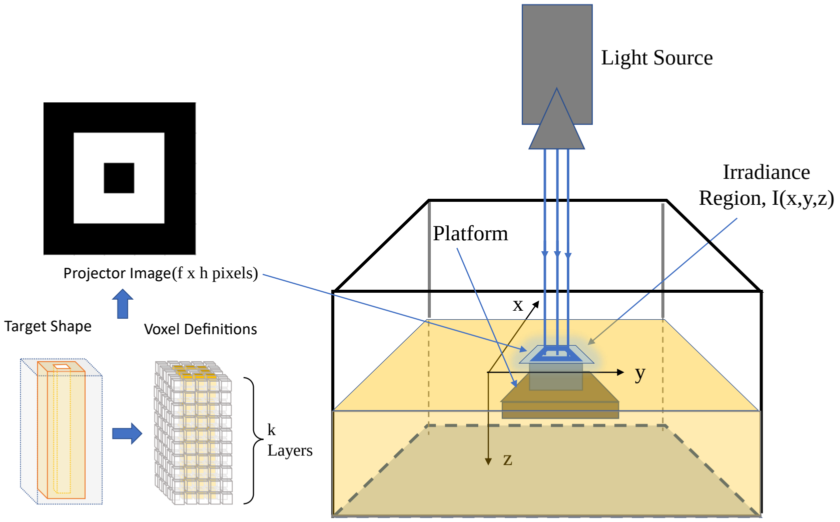

Figure 3.2: Irradiance of a square layer on a photo-polymeric resin surface.

In order to define the equations of the linear programming problem, the terms source pixel and target voxel need to be defined. Source pixels are the pixels projected onto the resin on each layer. Target voxels are the voxels that are meant to be cured. In Eq.(3.4), the effect of a single light beam generated from a source pixel on the corresponding layer image is calculated. Then, the total irradiance accumulated at a target voxel can be calculated as the sum of the irradiance from all the source pixels from the same or previous layer images. This value can be calculated by applying Eq.(3.4) to all layers and pixels with superposition as shown in Eq.(3.5).

$$I_{(i,j,k)} = \sum_{n=1}^{k} \sum_{m=1}^{f} \sum_{l=1}^{h} a_{(l,m,n)} \cdot e^{-\left(\frac{(i-l)^2}{2\sigma^2} + \frac{(j-m)^2}{2\sigma^2}\right)} \cdot 10^{-c(k-n)} \tag{3.5}$$

In Eq.(3.5), (l, m, n) index the (x, y, z) coordinates of the source pixels, and they were introduced to avoid confusion with the target voxel index (i, j, k). The energy absorbed by a voxel can be calculated by multiplying the total irradiance on that voxel by the exposure time, t (see Eq.(3.6)).

$$E_{(i,j,k)} = I_{(i,j,k)} \cdot t \tag{3.6}$$

The energy required to cure the resin is called the critical energy, E_c. If the energy absorbed by a voxel goes above the critical energy, the resin in that voxel cures. In continuous printing systems, the exposure time t is inversely proportional to the speed at which the platform moves vertically. In this system, the platform is lowered into the resin at a speed of $0.03 mm/s$. The speed of the platform has been chosen through experimentation, by inspecting the parts printed without optimization and determining at which speed the parts were most accurate and with least amount of defects. Layer thickness is $0.112 mm$, and the time it takes for the platform to move one layer (i.e., the exposure time) is $0.373 s$. The platform speed can be reduced to increase the exposure time, which effectively increases the energy absorbed by all voxels. Therefore, for a constant speed system, the energy distribution of any layer with size $f \times h$ can be written in matrix form as Eq.(3.7).

$$E(k) = t \cdot \begin{bmatrix} I_{(1,1,k)} & I_{(1,2,k)} & \cdots & I_{(1,h,k)} \\ I_{(2,1,k)} & I_{(2,2,k)} & \cdots & I_{(2,h,k)} \\ \vdots & \vdots & \ddots & \vdots \\ I_{(f,1,k)} & I_{(f,2,k)} & \cdots & I_{(f,h,k)} \end{bmatrix}_{f \times h} \tag{3.7}$$

Compiling the energy matrices for all layers into a 3D matrix gives the energy distribution model for a part. By comparing the elements of the energy matrices to the critical energy, E_c, the voxels that are cured can be identified, and the solidification model can be presented.

3.2 Identification of Parameters in the Solidification Model

The formulations given in Eq.(3.1)-Eq.(3.7) have various parameters that need to be identified before the solidification model is finalized. Controlled experiments were performed using our experimental setup shown in Figure 2.1.

The model parameters were determined by performing a series of experiments. First, the image shown in Figure 3.3 was projected onto the resin, and the light inside the resin was photographed from the side with a high-speed camera. Using a picture editing software, the pixels of this photograph with the highest light value of 255 were isolated. The plot formed by the boundary of these pixels was then compared to light distribution model results to fine-tune the constants, where the constants were determined as $c = 0.008\, m^{-1}$ and $\sigma = 13$. The images from this process can be found in Figure 3.4.

Figure 3.3: Image projected for the calibration of constants. Lit areas have 100%, 75%, 50% and 25% of the maximum light value 255, respectively.

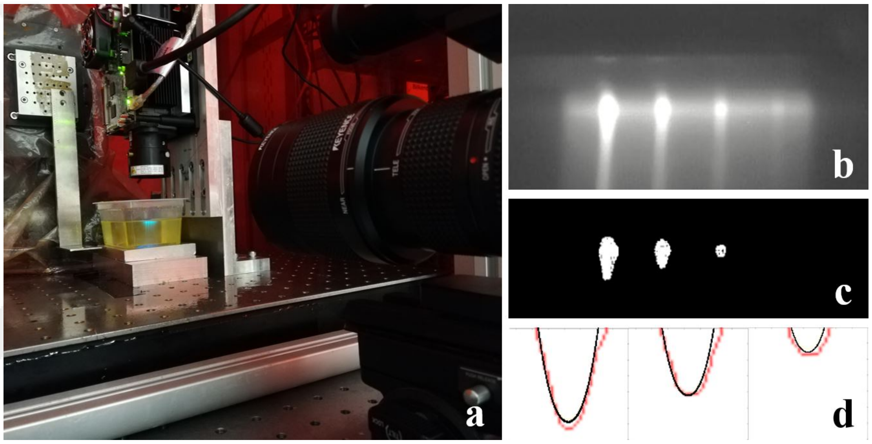

Figure 3.4: (a) Experiment setup with the high-speed camera directed at the resin vat as Figure 3.3 is projected onto the resin. (b) High-speed microscope image of light propagation in the polymer resin when Figure 3.3 is projected onto the surface. (c) Every pixel except those with value 255 has been omitted from A to be able to clearly distinguish the boundaries of a common energy value. The threshold value choice is arbitrary and could have been a value other than 255. (d) After examining how each variable in the model affects the curve's profile, the best set of variables has been chosen depending on how well they fit the experimental curves. Red lines are the experimentally acquired curves, and black lines are the numerical model.

It should be noted that in Figure 3.1, the cone shape profile is given as a visual representation of the area lit inside the resin. We assume that the absorption occurs at all points, at different intensities and with different magnitudes. In Figure 3.4, a threshold is selected to provide a profile on which all boundary points have the same intensity. The obtained profile is used for calibrating the parameters which are in turn used to calculate the intensity at all points in the resin using Equation 5. The choice of the threshold value is arbitrary and does not need to be 255. Choosing a different threshold value gives the profile of a different intensity value but the model parameters remain the same.

For comparison, an additional threshold value was chosen (marked as Threshold value 240) and the boundary profiles of the area projected with the maximum light value for both cases (Threshold value 240 and 255) were compared against the intensity profiles from the model (shown as isolines) in Figure 3.5 below.

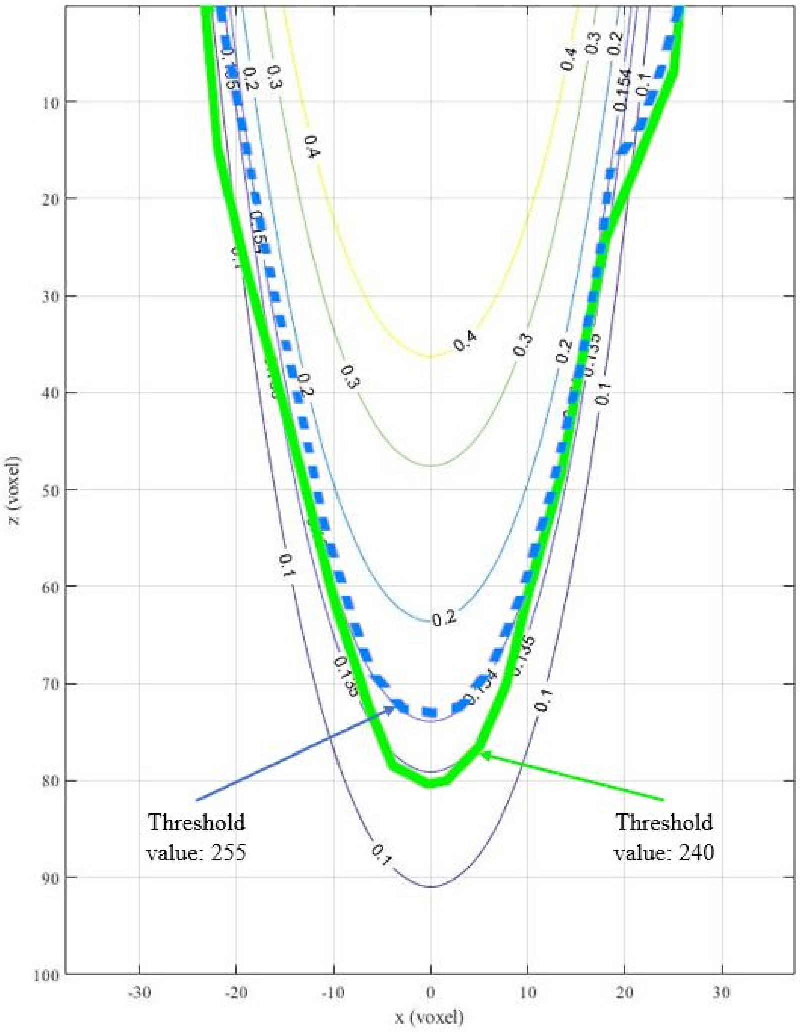

Figure 3.5: Boundary profiles obtained using threshold values 255 and 240 are given as lines colored blue (dashed) and green, respectively. Various normalized intensity lines with the same parameters were plotted for comparison.

As Figure 3.5 shows, selecting a different threshold value points to a different intensity level in the model without changing parameters.

Variables that are optimized for this study are the a values given in Eq.(3.5). Each source pixel has an a value for the amplitude of the Gaussian in the model, and these values depend solely on the grayscale value of the pixel. The energy absorbed by each pixel is a function of $\boldsymbol{a}$, the vector containing the a values of all source pixels. Therefore the optimization is formulated around $\boldsymbol{a}$. The grayscale values g were not used directly in the formulation in order to lower the computational load on the optimization process. $\boldsymbol{a}$ is a vector with elements valued between 0 and 3 and is related to the tone values of the pixels $\boldsymbol{g}$ (values between 0 and 255). As defined previously in Eq. (4.3), these values are related as in the equation in Figure 3.6. The value of γ was determined experimentally. From the three data points of 100%, 75% and 50% g and their corresponding a values, and also noting the plot starts from the origin, using Eq.(4.3) with $\gamma = 2.4040$ produces the curve that best fits the data, as can be seen in Figure 3.6.

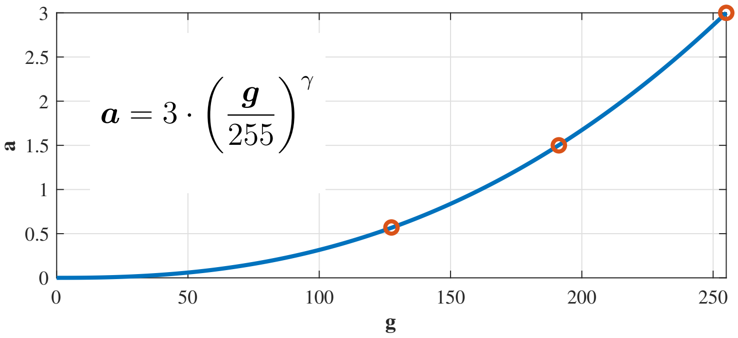

Figure 3.6: Plot of $\boldsymbol{g}$ vs $\boldsymbol{a}$. Orange colored dots are the data points.

After selecting the constants that best fit the light penetration images, the *dot test* was performed: The platform was fixed at $1mm$ below the resin surface, and a 50×50 pixel square was projected for 60 seconds. The results obtained were compared to the numerical model prediction, and the choice of constants was validated. Figure 3.7(a) shows the resulting built 3D part from this test. The yellow parabolic overlay is what the model calculated with the chosen constants.

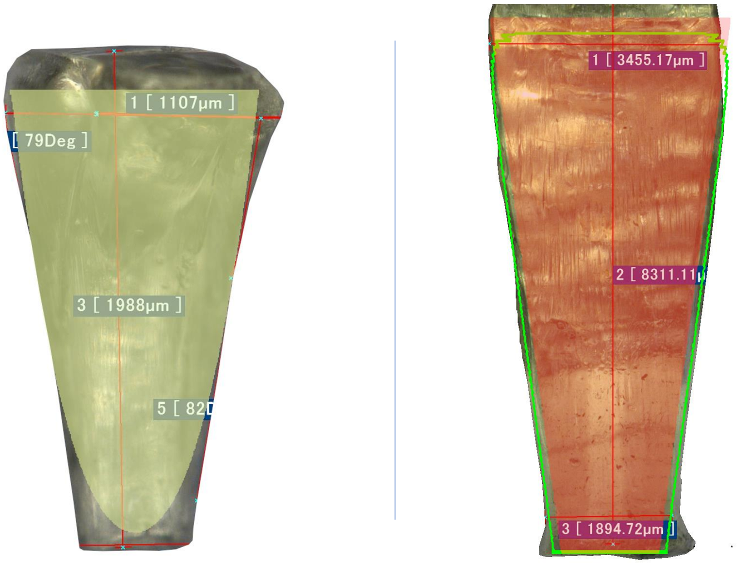

a

b

Figure 3.7: (a)Dot test result. The dome-like structure at the top is formed by the curing of resin pooled on top because of the capillary forces. This phenomenon occurred because the platform was stationary and would not occur in a regular process. (b) Test piece to help determine the critical energy. The red silhouette is the original CAD of the part. The green outline is the prediction of the model for this part.

As explained earlier in Section 3.1, the solidification model creates a 3D matrix containing values corresponding to the total energy each pixel absorbs during the print. After identifying the speed, a square prism tapered towards the bottom was built. This part is chosen intentionally so that a possible over-curing in print can be observed. In Figure 3.7(b), the red silhouette is the original part, the green outline is what the model predicted for the built product, and the piece in the background is the built part. The curing threshold value (critical energy) was determined by checking which isoline fits the built part. The green outline in Figure 3.7(b) was the closest to the built part. Therefore, this energy value was determined as the critical energy. The critical energy E_c of the resin at $444 - 465nm$ incident light has been calculated as $238J/cm^2$. This number is higher than expected due to working at a lower absorption wavelength region of the resin [5]. The effect of the low absorption due to wavelength variation on the critical energy has been demonstrated by Zhakeyev et al. in [41].

In order to include the effect of photobleaching, the absorption spectrum of the resin used in this study was measured before and after curing. The spectroscopy plots are given in Figure 3.8. An overall decrease in the absorption has been observed, while remaining relatively close in the wavelength range of the projector ($444-465nm$). The methodology used for determining and calibrating the model parameters includes the effect of photobleaching since cured parts are used along with the light profiles in the resin. It should be noted that the effects of photobleaching may be critical, and must be adjusted separately in the model if a light source with a different wavelength range was used.

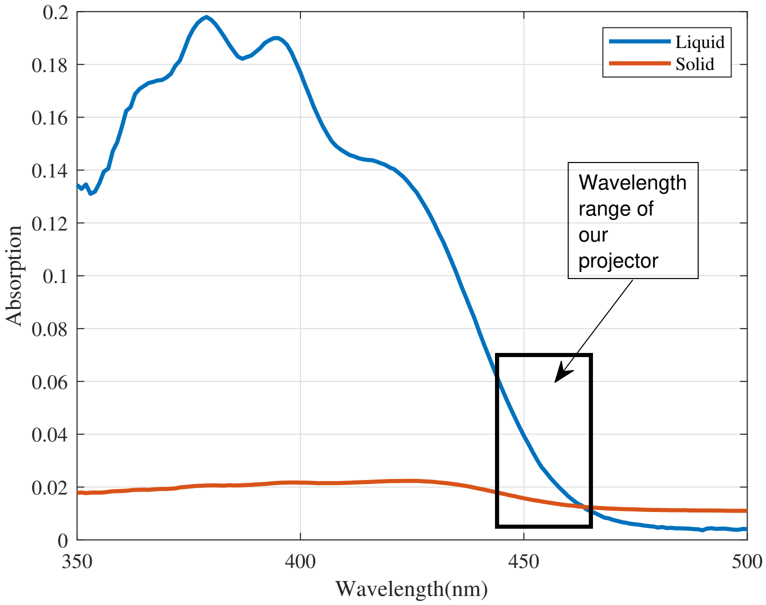

Figure 3.8: $350-500nm$ spectroscopy results for the polymer resin in liquid and solid form. The blue LED of the projector emits light in the $444-465nm$ range, the relevant region is marked with a black rectangle.

Chapter 4

Grayscale Optimization of Layer Images

Once a solidification model with specific parameters and variables is developed, improvements can be identified so that the manufacturing process can be performed better (for example, faster production with better quality). For complex systems and processes that have many variables, formulating and solving an optimization problem is a typical approach for finding a set of settings with the optimal performance. For most manufacturing processes, the objective is to minimize an accumulated error representing the deviation from the intended production properties. The solidification model developed in the previous chapter represents the basis for the problem constraints. This chapter aims to utilize grayscaling, which reduces the irradiance of light on a localized area, to reduce the accumulated error in manufacturing.

4.1 Model Based Process Optimization with Dynamic Programming

Following the same notation from before, Eq.(3.5) can be rewritten in the form

$$I_{(i,j,k)} = \sum_{lmn} a_{(l,m,n)} \cdot w_{(i,j,k,l,m,n)} \tag{4.1}$$

where w are irradiance model coefficients of the source pixels. Usign Eq.(4.1), the energy absorbed by a voxel at the coordinates (i, j, k) is defined in terms of a and w as Eq.(5.9).

$$E_{(i,j,k)} = t \cdot \sum_{lmn} a_{(l,m,n)} \cdot w_{(i,j,k,l,m,n)} \tag{4.2}$$

Each source pixel has a grayscale value g between 0 and 255, 0 representing black (no light) and 255 representing white (i.e., full intensity). Grayscale factor a of a pixel is defined as Eq.(4.3).

$$a = 3 \cdot \left(\frac{g}{255}\right)^{\gamma} \tag{4.3}$$

Value of γ will be determined experimentally. The pixel grayscale factor, a, is the design variable of our optimization problem. The objective function, $J(\boldsymbol{a})$, is the total energy absorbed by all boundary voxels as shown in Eq.(5.10). Boundary voxels are voxels next to target voxels and are intended to remain uncured.

$$J(\boldsymbol{a}) = \sum_{d=1}^{D} E_d(\boldsymbol{a}) \tag{4.4}$$

where D is the number of boundary voxels and $\boldsymbol{a}$ is the vector containing the grayscale factor values for all source pixels. E_d is the energy absorbed by a boundary voxel.

The formulation for the grayscale optimization problem can be written as shown in Eq.(5.11).

$$\min_{a} J(\boldsymbol{a}) \text{ such that } \begin{cases} \boldsymbol{A} \cdot \boldsymbol{a} \leq \boldsymbol{b} \\ \boldsymbol{lb} \leq \boldsymbol{a} \leq \boldsymbol{ub} \end{cases} \tag{4.5}$$

where $\boldsymbol{lb}$ and $\boldsymbol{ub}$ are the lower and upper bound of values elements of $\boldsymbol{a}$ can have. The goal of the optimization is to minimize the objective function $J(\boldsymbol{a})$ while keeping the energy values of target voxels above the critical energy. This allows the part to be built with high accuracy, using as little energy as possible.

When the target voxel located at (i, j, k) needs to cure as part of the production, the inequality constraint given in Eq.(5.12) must be satisfied.

$$E_{(i,j,k)} \geq E_c \tag{4.6}$$

For successful production of a part, each target voxel needs to cure when the process finishes. This collection of constraints can be represented in our formulation by calculating a matrix $\boldsymbol{A}$, each row of which can be written as shown in Eq.(4.7).

$$\boldsymbol{A}_r = \boldsymbol{A}_{(i,j,k)} = -t \cdot [\, w_{(i,j,k,1,1,1)} \;\; w_{(i,j,k,1,1,2)} \;\; \cdots \;\; w_{(i,j,k,1,3,n)} \;\; \cdots \;\; w_{(i,j,k,l,m,n)} \,]_{1\times q} \tag{4.7}$$

$\boldsymbol{A}$ is a $p \times q$ matrix where p is the number of inequality constraints (i.e. the number of target voxels), and q is the number of variables (i.e. the number of source pixels). Each row of $\boldsymbol{A}$ has a corresponding value in vector $\boldsymbol{b}$ with p elements (see Eq.(4.8)).

$$b_r = [b_{(i,j,k)}] = -E_c \tag{4.8}$$

Note the minus sign in Equations Eq.(4.7) and Eq.(4.8), since the optimization formulation needs to be a $\leq$ inequality; both sides of Eq.(5.12) are multiplied by -1 to reverse the sign.

Because of the large number of linear relationships existing in the model developed in Eq.(3.1)-Eq.(3.7) and considering the vast availability of tools in literature, the optimization problem is formulated as a linear programming problem.

After the objective function and the constraint equations are formulated, Matlab Optimization Toolbox is used for solving the actual optimization problem.

The formulation of the optimization problem and remapping of the results to slice image form is summarized in the workflow shown in Figure 4.1.

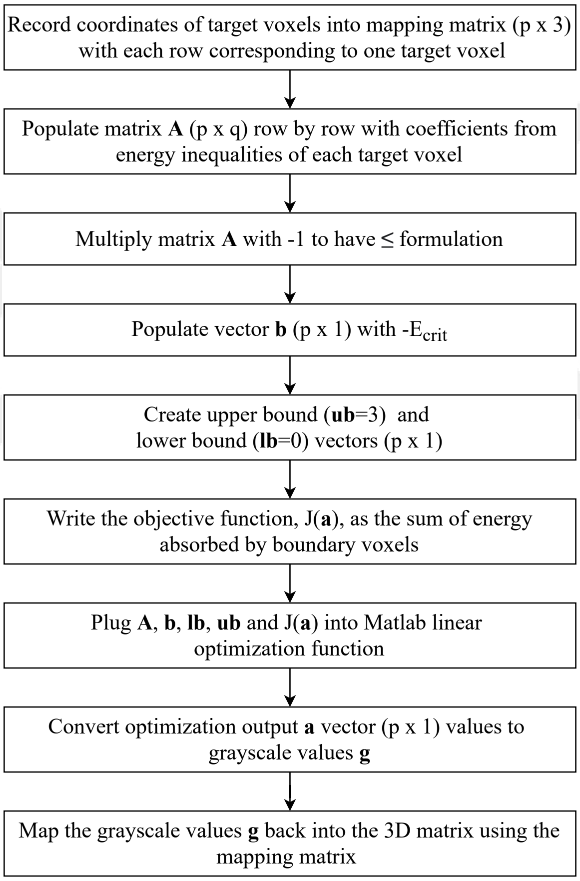

Figure 4.1: Optimization flowchart explaining the steps followed to optimize any part to be built.

An example of optimizing a simple part is provided in 4.1.1 to help understand the optimization process.

4.1.1 Simple Optimization Example

In Section 3.1, a mathematical solidification model for the VPP process was presented. In Section 4.1, this model was used to improve the dimensional accuracy of the printing process by use of linear programming optimization techniques. The VPP process utilizes multiple layer images represented in terms of matrices in the formulations. Typically, these matrices and vectors are too big to present on paper, even for a simple part.

In order to give an outline of how the optimization problem is formulated and the energy and grayscale values are affected during the optimization, an example of a 5-pixel diameter cylinder with a height of 5 layers will be provided here.

The object is broken into voxels as seen in Figure 4.2(a). The cylinder 5 layers in height and 5 pixels in diameter is assumed to be contained in a volumetric box of $7 \times 7 \times 5$ voxels. Since the cylinder has a uniform cross-sectional area, the layer image is the same for all layers. It is important to note that although the cylinder has a perfectly circular cross-section, the layer image shown in the projector will be imperfect with a pixelated version. The more pixels used, the better the quality of the image. Figure 4.2(b) shows the target voxels and the boundary voxels used for a layer during optimization.

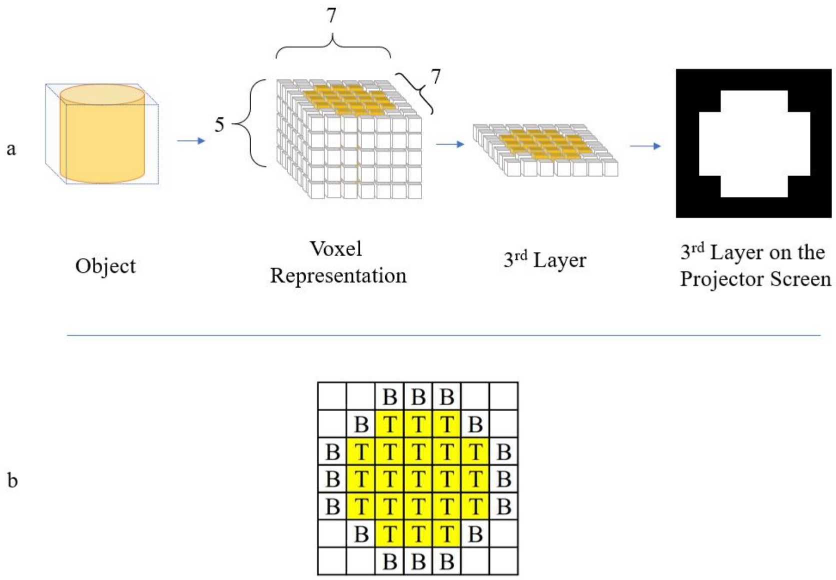

		B	B	B		
	B	T	T	T	B	
B	T	T	T	T	T	B
B	T	T	T	T	T	B
B	T	T	T	T	T	B
	B	T	T	T	B	
		B	B	B		

Figure 4.2: (a) Simple cylinder example. (b) Boundary and target voxels in a layer. B are boundary voxels and T are target voxels.

Initially, the object is sliced into layers using ".png" images with white pixels where the part needs to be cured and black where it should not. Every initial image of this object is the same; see the left column of Figure 4.3. Starting from the initial layer images, the $\boldsymbol{A}$ matrix is formulated as explained in section 4.1. The matrix $\boldsymbol{A}$ is 105×105, and it is too large to present fully here. Instead, one row of the matrix $\boldsymbol{A}$, corresponding to the voxel at $(3, 3, 3)$ is given in Eq.(4.9). Calculation of this row can be followed from Eq.(3.5) and Eq.(4.7).

$$
\begin{aligned}
\boldsymbol{A}_{(3,3,3)} = [&0\ 0\ 0\ 0\ 0\ 0\ 0\ 0\ 0\ 0\ 0\ 0\ 0\ 0\ 0\ 0\ 0\ 0\ 0\ 0\ 0\ 0\ 0\ 0\ 0\ \ldots \\
&\ldots\ 0\ 0\ 0\ 0\ 0\ 0\ 0\ 0\ 0\ 0\ 0\ 0\ 0\ 0\ 0\ 0\ 0\ \ -0.985\ \ -0.988\ \ldots \\
&\ldots\ \ -0.985\ \ -0.985\ \ -0.994\ \ -0.997\ \ -0.994\ \ -0.985\ldots \\
&\ldots\ \ -0.988\ \ -0.997\ \ -1\ \ -0.997\ \ -0.988\ \ -0.985\ \ -0.994\ \ldots \\
&\ldots\ \ -0.997\ \ -0.994\ \ -0.985\ \ -0.985\ \ -0.988\ \ -0.985\ \ -0.967\ \ldots \\
&\ldots\ \ -0.970\ \ -0.967\ \ -0.967\ \ -0.976\ \ -0.979\ \ -0.976\ \ -0.967\ \ldots \\
&\ldots\ \ -0.970\ \ -0.979\ \ -0.981\ \ -0.979\ \ -0.970\ \ -0.967\ \ -0.976\ \ldots \\
&\ldots\ \ -0.979\ \ -0.976\ \ -0.967\ \ -0.967\ \ -0.970\ \ -0.967\ \ -0.950\ \ldots \\
&\ldots\ \ -0.952\ \ -0.950\ \ -0.950\ \ -0.958\ \ -0.961\ \ -0.958\ \ -0.950\ \ldots \\
&\ldots\ \ -0.952\ \ -0.961\ \ -0.964\ \ -0.961\ \ -0.952\ \ -0.950\ \ -0.958\ \ldots \\
&\ldots\ \ -0.961\ \ -0.958\ \ -0.950\ \ -0.950\ \ -0.952\ \ -0.950\,]_{1\times 105}
\end{aligned}
\tag{4.9}
$$

The zeros in the row correspond to the source pixels in the layers below the chosen voxel. These sources do not affect the energy absorbed by the voxel; therefore, their values are set to zero. The only source with the value -1 is the source pixel that is coincident with the chosen voxel. Afterwards $\boldsymbol{b}$, $\boldsymbol{ub}$, $\boldsymbol{lb}$ and $E(\boldsymbol{a})$ are calculated. $\boldsymbol{b}$ and $E(a)$ are calculated through Eq.(4.8) and Eq.(5.10) respectively. For this example, the critical curing energy E_c was taken to be 170. $\boldsymbol{ub}$ and $\boldsymbol{lb}$ are the same in all versions, as values of $\boldsymbol{a}$ are between 0 and 3.

$$
\boldsymbol{b} = \begin{bmatrix} -170 \\ -170 \\ \ldots \\ -170 \\ -170 \end{bmatrix}_{105\times 1}
\tag{4.10}
$$

The optimization is performed, and the $\boldsymbol{a}$ vector containing the a values for all source pixels is obtained. This vector is transformed into the $\boldsymbol{g}$ vector using Eq.(4.3) and new images are constructed by mapping the values of the $\boldsymbol{g}$ vector back to the corresponding pixels. The result of this process is given on the right column of Figure 4.3.

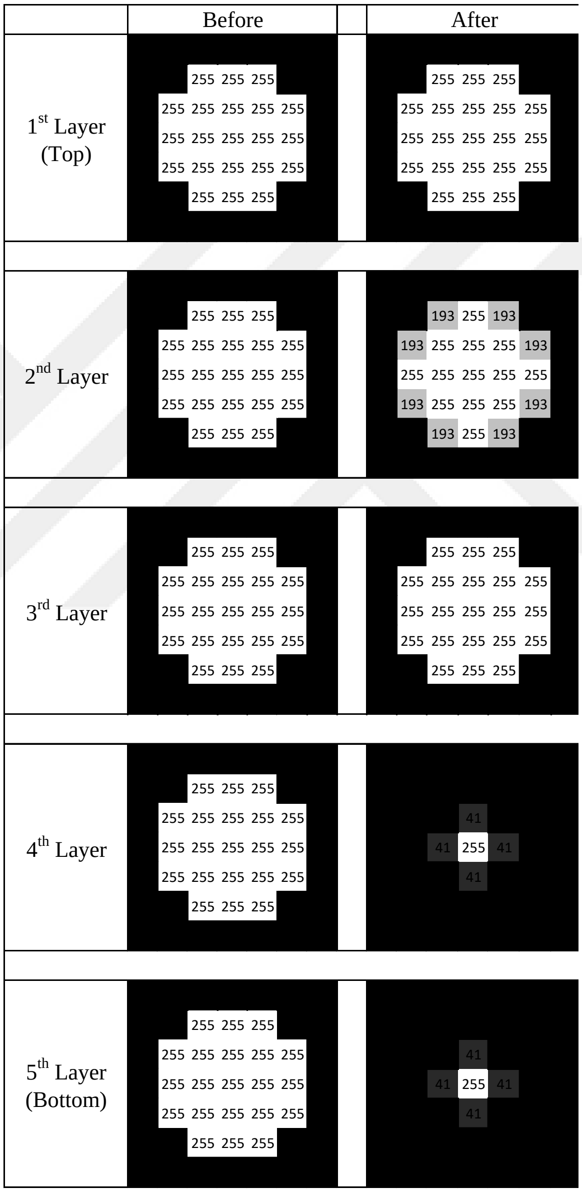

Figure 4.3: Light value of each projected pixel, before and after optimization.

Notice that the optimization algorithm greys parts of the 2^{nd} Layer, but the 1^{st} and 3^{rd} Layers receive full exposure. In the proposed optimization procedure, the few layers at the top of any part need full exposure as the light from a few layers is not enough to cure the desired voxels. This dictates how the target voxels are selected. Voxels that need to be cured are selected as targets if they receive more energy than E_c in the simulation without optimization. Since the underexposed voxels are not designated as targets, the optimization algorithm can occasionally decrease the light at the top layers slightly even though ideally it should be full exposure for the best overall result. Therefore, the topmost layers of a part may not be accurate. This issue will be addressed in future work.

In Figure 4.4, the energy absorbed by the voxels in the third layer before and after optimization is given. The third layer was chosen because the top layers usually cannot get enough energy to go above the critical energy, and the lower layers produce very similar results and do not add anything of significance to the discussion. Following the color pattern from Figure 4.2, voxels marked yellow go above the critical energy and are thus cured. White voxels absorb less energy than critical energy and remain uncured. Having voxels that should not be cured marked yellow means an over-curing problem in those voxels.

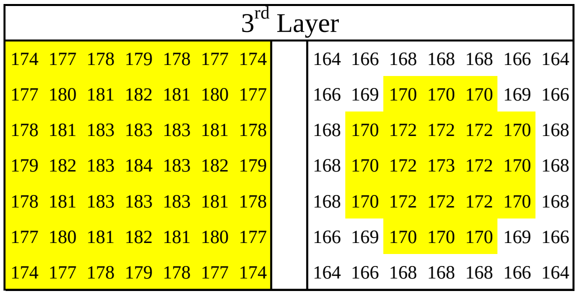

3^{rd} Layer														
174	177	178	179	178	177	174		164	166	168	168	168	166	164
177	180	181	182	181	180	177		166	169	170	170	170	169	166
178	181	183	183	183	181	178		168	170	172	172	172	170	168
179	182	183	184	183	182	179		168	170	172	173	172	170	168
178	181	183	183	183	181	178		168	170	172	172	172	170	168
177	180	181	182	181	180	177		166	169	170	170	170	169	166
174	177	178	179	178	177	174		164	166	168	168	168	166	164

Figure 4.4: Energy absorbed by each voxel in the third layer, before and after optimization.

The simulation suggests that using the layer images produced by the optimization algorithm fixes the overcuring issue and ensures the curing of only the intended voxels.

In an ideal case, all pixels on all the images would be sources, and every voxel in the CAD part would be a target. However, typically, there are computational limitations. Choice of targets and sources along with some basic techniques to improve the computational efficiency of the problem are explained in 4.1.2.

4.1.2 Sources, Targets and Segmentation

Ideally, all pixels would be sources, and all voxels of the CAD part would be targets. However, each source adds an extra variable to be optimized. Increasing the number of sources or targets enlarges the matrices put into the optimization algorithm. If these matrices become too large, the computational power required becomes immense.

The memory capacity of the computer performing the optimization can be a serious bottleneck in terms of the number of variables that can be optimized at once. Depending on the size of the part, it may not be possible to optimize all pixels and voxels at once. This makes the choice of sources and targets crucial. Since over-curing is a more prevalent issue than under-curing, only the lit pixels in the layer images were chosen as sources. The coincident voxels that absorb more energy than the critical threshold with unedited images are selected as the targets.

If there are still too many variables after the choice of targets and sources, the part is divided into small segments to be optimizable. Steps followed in how a part is divided into segments are shown in the flowchart in Figure 4.5.

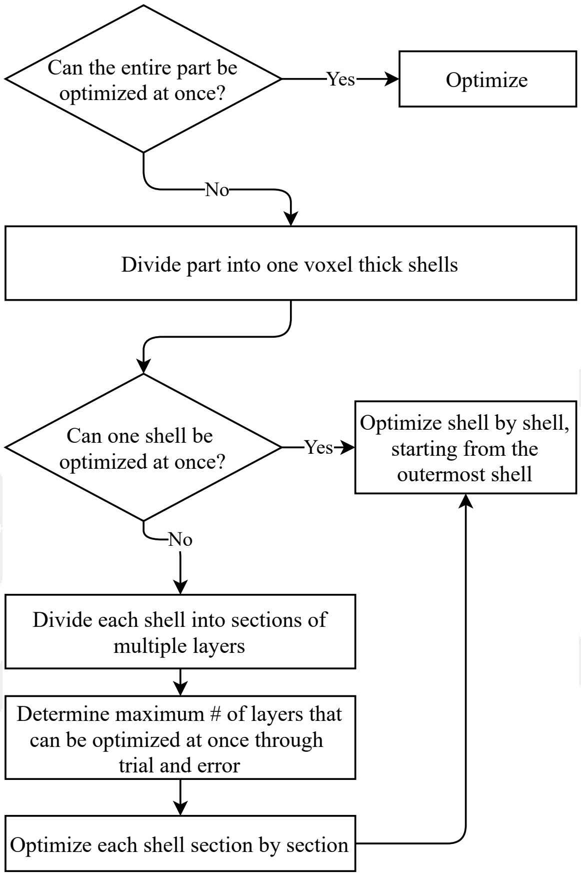

Figure 4.5: Segmentation flowchart.

The part is first split into shells. These shells fit into each other and make up the 3D part, much like the layers of an onion. Those shells are then split into sections of multiple layers to lower the computation load. In the case of the DNA part example, 30 layers were used. The 30-layer sections have 50% overlap, meaning every single layer is part of two adjacent segments. (Section1: layers 1-30, Section 2: layers 16-45 ...) Increasing the overlap of the sections result in a more uniform optimization result. This overlap decreases the error caused by the segmentation by 18%.

4.2 Validation of the Optimization Method

The method outlined in Section 4.1 promises significant improvements regarding the shape of the resulting part after model-based image layer optimization. To test these improvements, a popular benchmark part shown in Figure 4.6 was manufactured using the optimization of projected images discussed in the previous section. The same part was also built without the optimization to compare how well it works and to validate its feasibility for practical components. Optimization and print results for a relatively simpler part have been provided in 4.2.1.

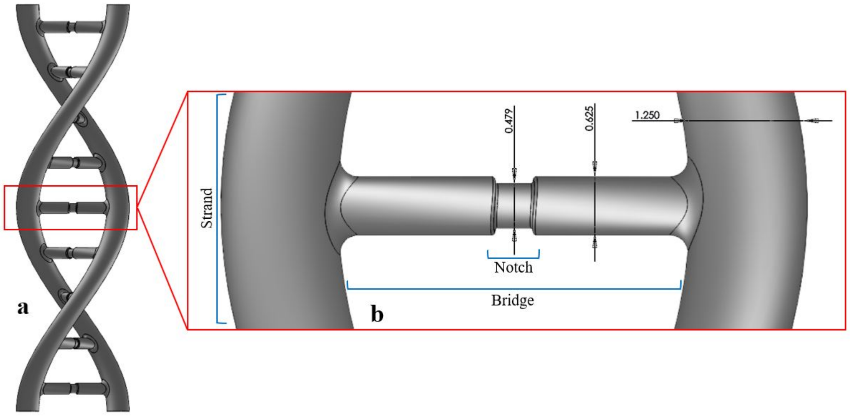

Figure 4.6: (a) CAD model of a DNA double helix part. (b) The close-up of a single nucleotide bridge section. Dimensions are in mm.

The *DNA double helix part* shown in Figure 4.6 is selected to test the real-life challenges of additive manufacturing as the nucleotide bridges in DNA allow for the common curing defects such as over-curing and thickness inaccuracy in overhanging structures. Since the feature repeats itself, our validation study focuses on optimizing a single section with one nucleotide bridge to speed up the computations and the manufacturing process. The results of this study can still be used for the whole part because the bridges are far enough apart that their effect on each other is negligible. The notch in the middle of the bridge in the CAD model adds complexity to the part to be produced, testing the capabilities of the proposed optimization method.

The accuracy of the model should be validated before moving on with the optimization. To compare the print simulation and the actual print, the DNA was simulated and printed with no alterations to its layer images. Images of the simulated part and the print are given in Figure 4.7. The 3D model is obtained as a Matlab volume graph by using the voxels that are identified as cured in the solidification model. The profile of the thinner middle section and the general dimensions of the simulation closely resemble those of the built part. The model accurately predicts how the final build is going to appear when the determined printing parameters are used.

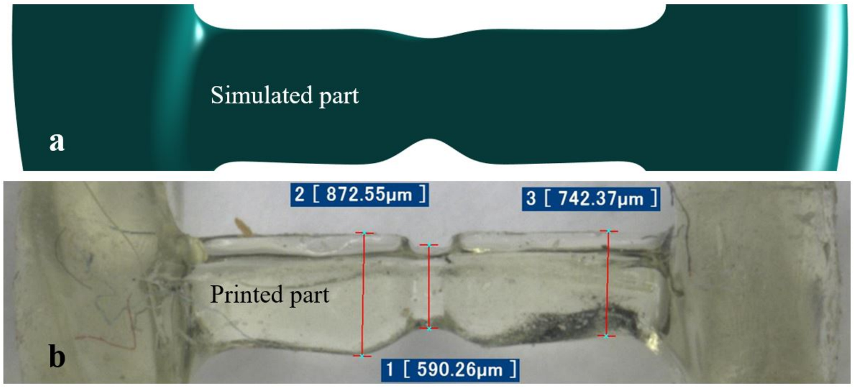

Figure 4.7: (a) Numerical model of a nucleotide bridge of a DNA molecule. (b) The print result of the same part.

In order to put the scale of the part into perspective, an image of the DNA part printed without optimization next to a 1 TRY coin has been provided in Figure 4.8.

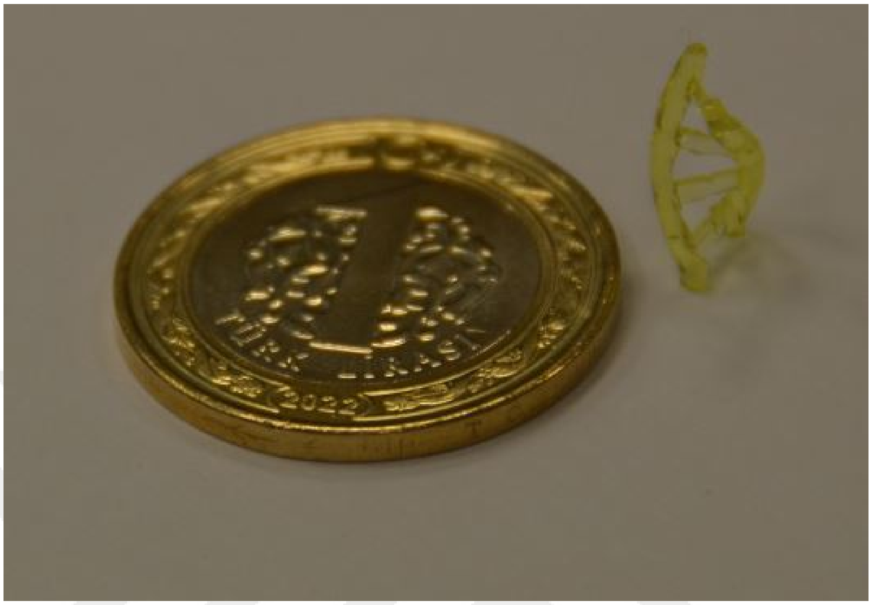

Figure 4.8: Printed DNA molecule next to 1 TRY coin.

In order to rapidly estimate the benefit of the optimization method, the mathematical model developed in Section 3.1 is used to simulate the manufacturing process with and without the optimization of the layer images. These simulation results are presented in Figure 4.9 and Figure 4.10. Figure 4.9(b) and Figure 4.9(c) show how the built part is expected to come out without and with the layer optimization, respectively. The prediction before the optimization in Figure 4.9(b) shows over-curing on the underside of the bridge. With optimization, this problem has been fixed, and the top part of the notch section became more defined. Figure 4.10 shows the simulation results from the top, where a slight reduction in the bridge thickness observed in Figure 4.10(b) is reduced after optimization as shown in Figure 4.10(c). The simulation results suggest an 11% decrease in the overall volume of the considered DNA section, going from $7.5mm^3$ to $6.7mm^3$.

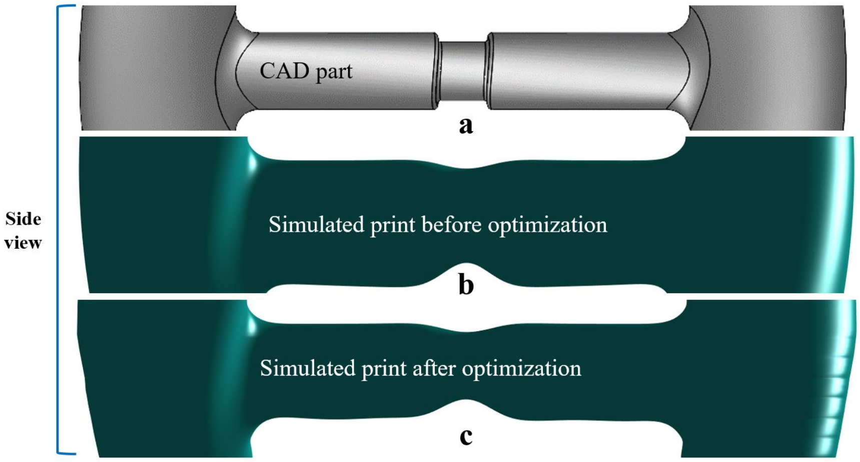

Figure 4.9: (a) Side view of the DNA section CAD model. (b) Side view of the print simulation before optimization. (c) Side view of the print simulation after optimization.

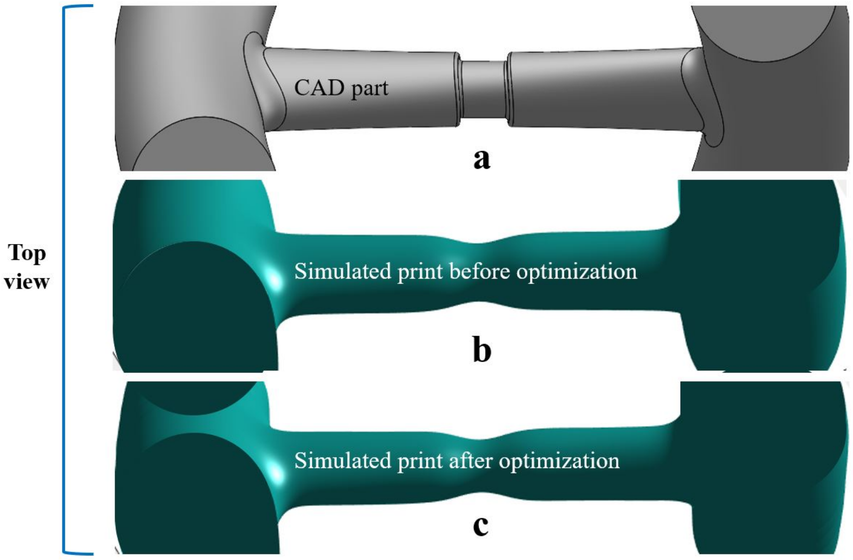

Figure 4.10: (a) Top view of the DNA section CAD model. (b) Top view of the print simulation before optimization. (c) Top view of the print simulation after optimization.

The predicted simulation results show promising improvements as shown in Figure 4.9 and Figure 4.10. Therefore, actual benchmark parts are produced in the VPP machine to verify if the predicted benefit in simulations is obtained. Figure 4.11 and Figure 4.12 show how the benchmark part is built before and after the optimization, respectively. Without the optimization, the part is overall thicker than it is supposed to be, the bottom profile of the bridge is distorted with a significant increase in thickness near the notch, and the top side of the connection between the bridge and the main strands is sharper. The thickness in the optimized part is much closer to the original CAD model shown in Figure 4.6, with the thickness of the notch in this specific example being 495 microns after optimization, 590 microns without the optimization as compared to the 479 microns from the targeted CAD drawing. The bottom profile was straightened out, and the bridge to main strand connections was smoothed out.

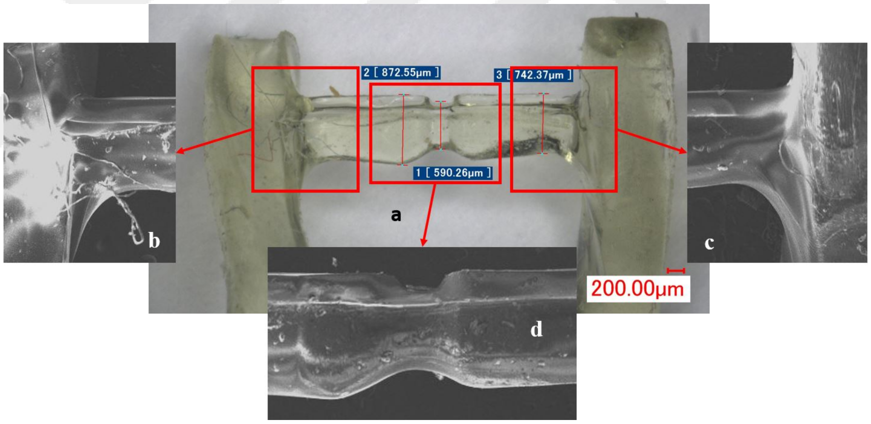

Figure 4.11: (a) Side view of print of the DNA section before optimization. (b) The E-SEM image close-up of the left bridge-strand connection. (c) The E-SEM image close-up of the right bridge-strand connection. (d) The E-SEM image close-up of the middle section.

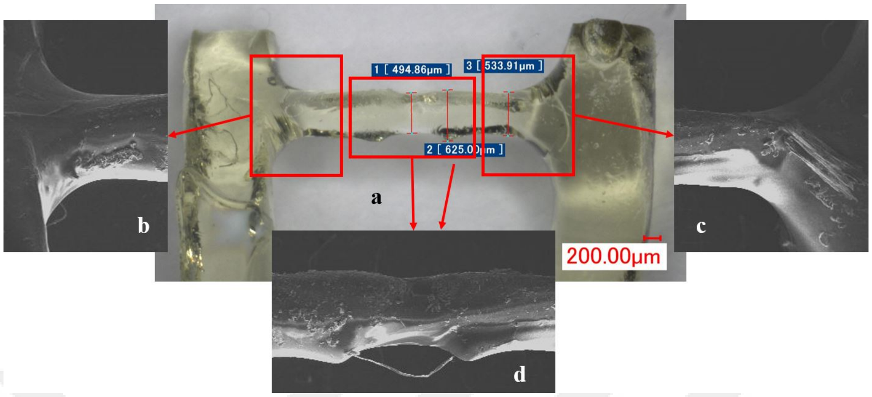

Figure 4.12: (a) Side view of optimized print of the DNA section. (b) The E-SEM image close-up of the left bridge-strand connection. (c) The E-SEM image close-up of the right bridge-strand connection. (d) The E-SEM image close-up of the middle section.

The grayscale images of the parts were obtained using the environmental scanning electron microscope (E-SEM) mentioned in Section 2.1. Figure 4.13 shows the built parts from the top in detail using an SEM. When built parts are observed from the top, the improvement caused by the optimization can be seen clearly. The overall profile was improved noticeably on both sides, and the sharp-edged sections on the top (middle in this image due to it being the top view) of the part were smoothed out by the optimization.

Figure 4.13: (a) Top E-SEM view of the DNA section before optimization. (b) Top E-SEM view of the optimized DNA section.

Figure 4.14 and Figure 4.15 show how two layers of the part were changed by the optimization. The layer considered in Figure 4.14 is from the underside of the bridge. Optimization darkened the middle section around the notch. This means that the energy absorbed from the upper layers' projection is enough to cure the middle section for this and the following layers. Notice that the section of the bridge just before connecting to the main strand is lit. This is important as it is a clear example of how optimization solves issues in the part. In Figure 4.11, the underside profile of the bridge is thinner closer to where the bridge connects to the strands and gets thicker towards the middle. Since the overall structure is thicker and needs to be thinned down, these connections are at the risk of becoming too thin. To offset the excessive thinning in these areas, the optimization left the parts of the layer image that correspond to these areas lit while darkening the middle section. This results in the problematic areas absorbing more energy and having more voxels cured, in turn achieving a more uniform shape with an accurate thickness, as can be seen in Figure 4.12. Layer in Figure 4.15 is from the middle of the bridge. There is slight graying or blacking out of regions, making the final shape thinner. Notice in both cases, the image is no longer symmetric after optimization. The helical structure of the DNA causes the parts that end up underneath the strands to overcure. Likewise, the opposing sides are more prone to undercuring. Therefore, parts of the images that correspond to the bottom sides of the strands are darker after optimization.

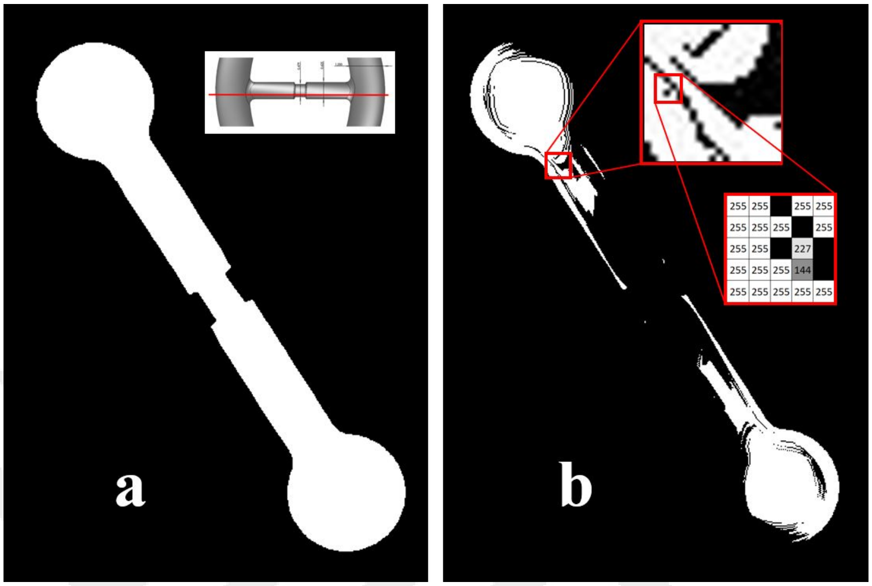

Figure 4.14: (a) A projected layer image near the bottom of the bridge, before optimization. Image on the top right shows where in the part this layer is located. (b) Image of the same layer after optimization.

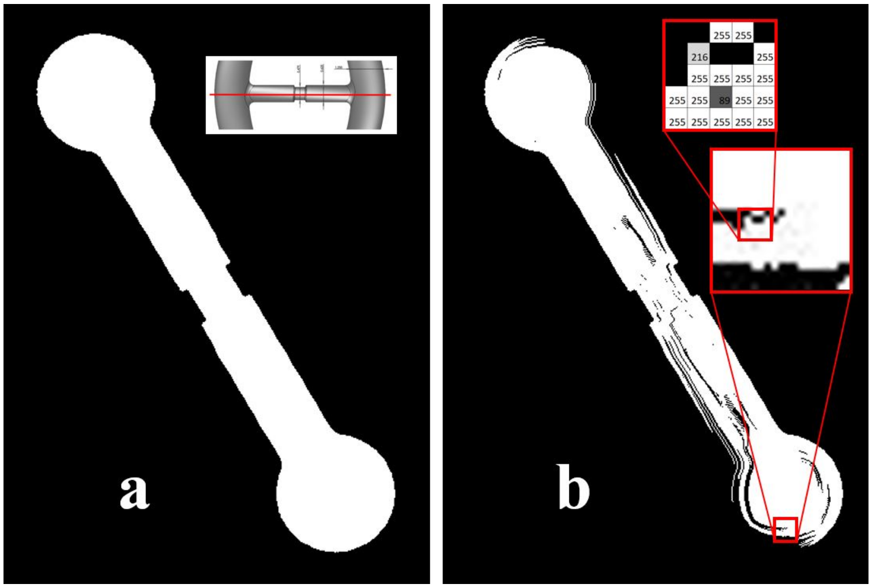

Figure 4.15: (a) A projected layer image at the middle of the bridge, before optimization. Image on the top right shows where in the part this layer is located. (b) Image of the same layer after optimization.

The simulation results show that there is a 24.7% decrease in the number of overcured voxels due to the optimization. A more robust selection of sources can decrease the overcured voxel count further, as described in 4.1.2.

Multiple parts were built with and without optimization, and notch thickness values were averaged. The average notch thickness before the optimization is 587 microns with a standard deviation of 72.3. For parts built without optimization, measured values along with their average and the target dimension is given in Figure 4.16(a). The average notch thickness after optimization is 476 microns with a standard deviation of 29.5. For optimized parts, measured values along with their average and the target dimension is given in Figure 4.16(b).

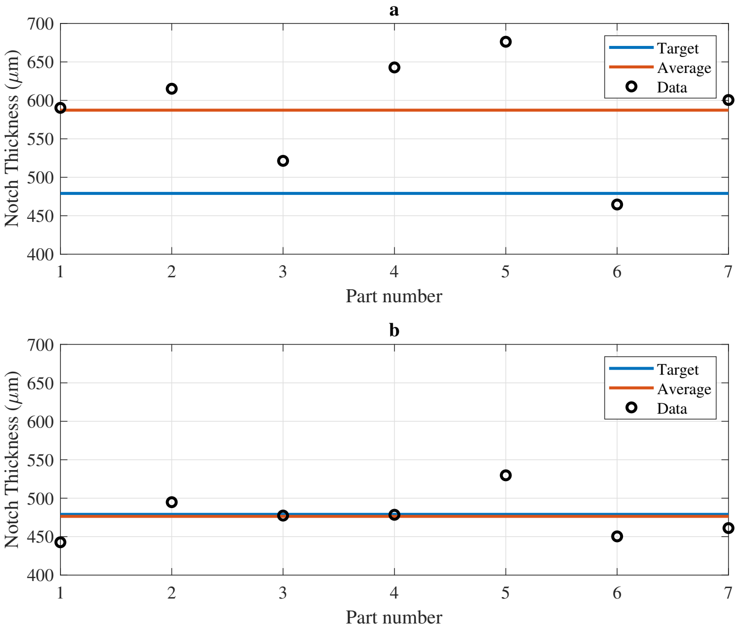

Figure 4.16: (a) Notch thickness values for parts built without optimization. (b) Notch thickness values for optimized built parts. The blue line is the targeted dimension, black dots are the measured notch thickness values and orange lines are the averages of the measured values.

Figure 4.16 shows that the optimization not only improved the dimensional accuracy of the part and it also reduced the variance in the data set.

4.2.1 Simple Part with Overhang

Parts with uniform overhanging slopes at angles 30, 45 and 60 degrees have been simulated, optimized and printed.

Simple micro-scale parts with uniform overhanging slopes at angles 30, 45 and 60 degrees were simulated and printed first without any alterations, and then again after the layer images had been optimized. The CAD drawings of the parts are given in Figure 4.17. Figure 4.18 shows the improvement caused by the optimization by comparing the simulations with and without the optimization. Red areas depict the areas that would have been overcured if the optimization had not been performed.

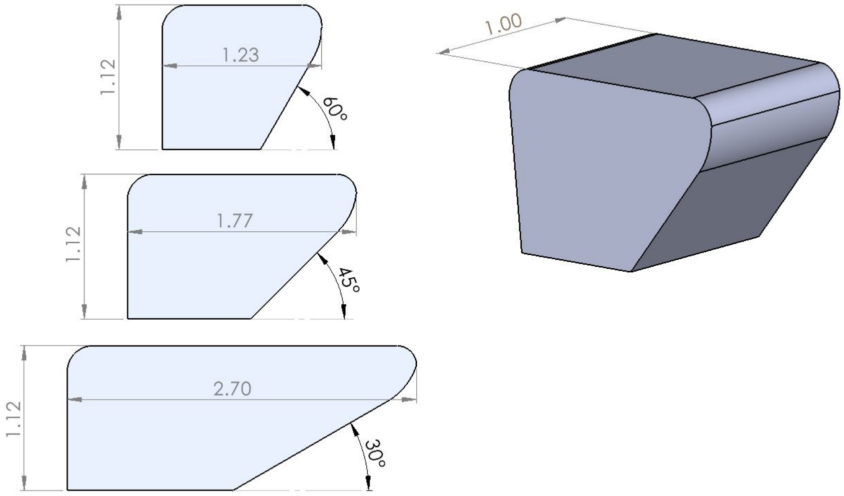

Figure 4.17: Side views of the parts with uniform overhanging slopes at 30, 45 and 60, along with the isometric view of the 45 part. Dimensions are in mm. The height corresponds to 100 layers.

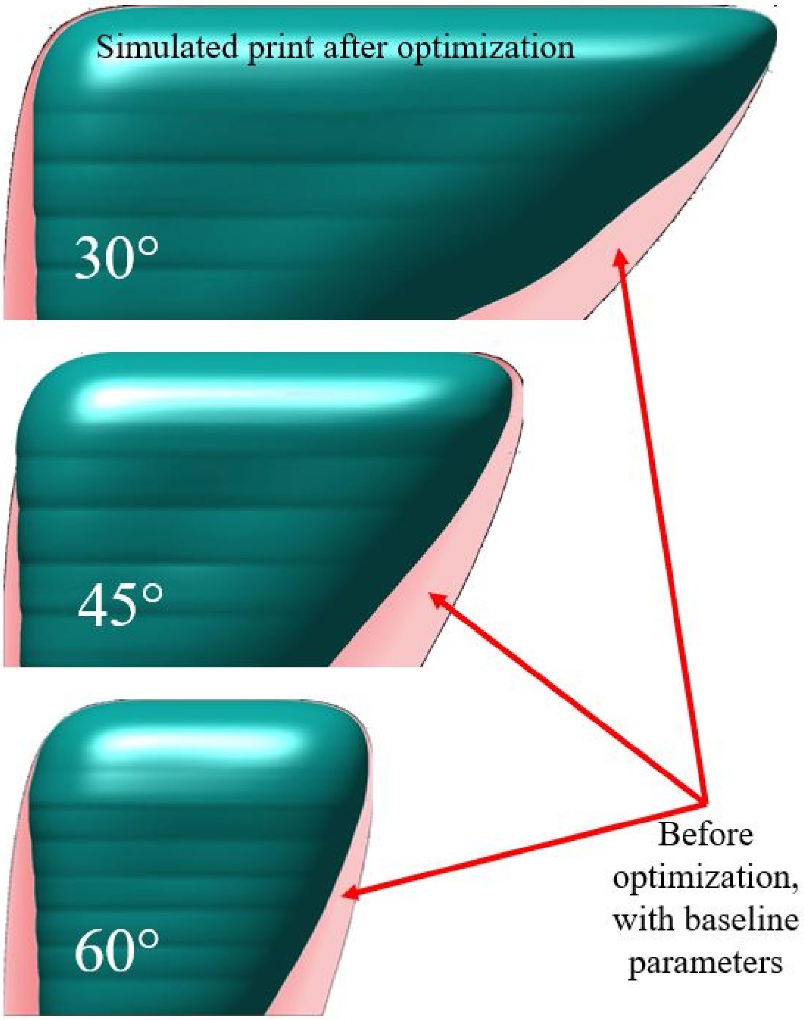

Figure 4.18: Simulated improvement on the print accuracy of all three parts. The green part is the simulated result after optimization, the red area is the predicted overcuring without the optimization.

The print results are presented and compared with the simulated parts in Figure 4.19, Figure 4.20 and Figure 4.21.

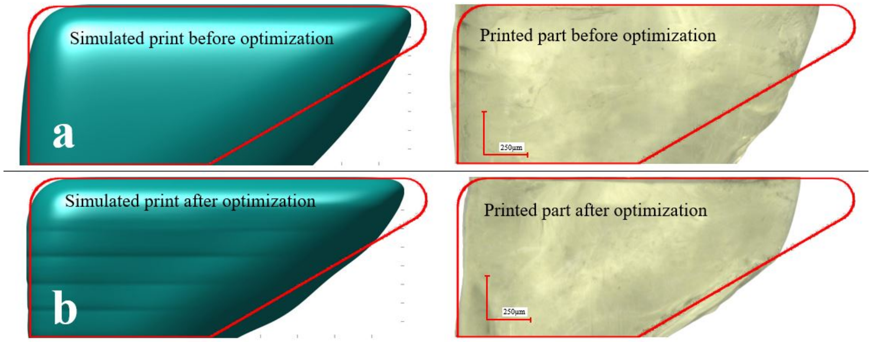

Figure 4.19: (a) Print simulation (left) and the print result (right) of the 30 part without optimization. (b) Print simulation (left) and the print result (right) of the 30 part with optimization. The red outline is the perimeter of the cad drawing and represent the intended profile for this print. The horizontal lines seen on the optimized simulation are a result of the segmentation. They do not have a considerable effect on the final print, evidenced by their absence on the printed part.

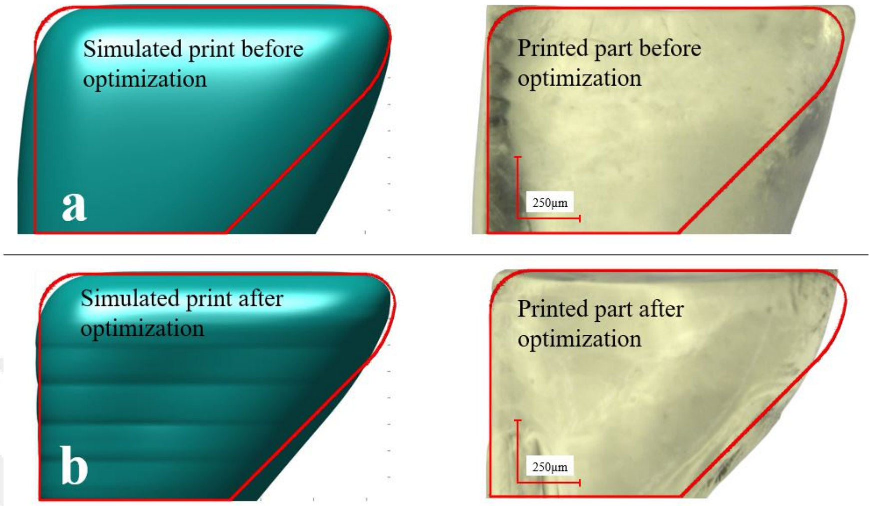

Figure 4.20: (a) Print simulation (left) and the print result (right) of the 45 part without optimization. (b) Print simulation (left) and the print result (right) of the 45 part with optimization. The red outline is the perimeter of the cad drawing and represent the intended profile for this print. The horizontal lines seen on the optimized simulation are a result of the segmentation. They do not have a considerable effect on the final print, evidenced by their absence on the printed part.

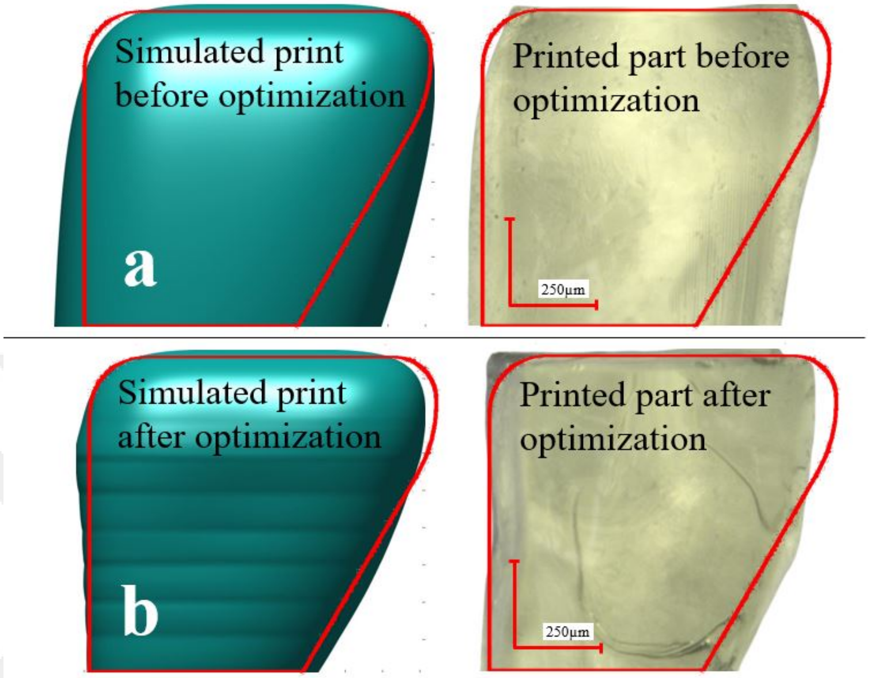

Figure 4.21: (a) Print simulation (left) and the print result (right) of the 60 part without optimization. (b) Print simulation (left) and the print result (right) of the 60 part with optimization. The red outline is the perimeter of the cad drawing and represent the intended profile for this print. The horizontal lines seen on the optimized simulation are a result of the segmentation. They do not have a considerable effect on the final print, evidenced by their absence on the printed part.

Along with the model simulation being accurate in estimating how a print will turn out, the optimization has improved the part accuracy significantly. The overcuring under the overhang and on the left side of the parts was reduced. Sizes of the overcured areas under the slopes for the simulations and the printed parts are given in table 4.1.

Overcured area under slope (mm^2)	30	45	60
Simulation before optimization	10.8×10^{-2}	19.1×10^{-2}	21.6×10^{-2}
Simulation after optimization	2.7×10^{-2}	4.5×10^{-2}	7.2×10^{-2}
Print before optimization	8.5×10^{-2}	23.5×10^{-2}	22.5×10^{-2}
Print after optimization	4.2×10^{-2}	5.6×10^{-2}	10.1×10^{-2}

Table 4.1 Areas under the slope that is overcured with respect to the intended CAD of the part.

Chapter 5

Variable Print Speed Optimization

Optimizing the platform speed during printing can offer a degree of control that was previously lacking and allow for production of parts with a wider range of geometries. Speeding up or slowing down the print at critical sections of the part allows for finer control on the energy absorbed by the resin on a layer by layer basis. Combined with the grayscale optimization explored in the earlier chapters, this approach improves the dimensional accuracy of printed parts significantly.

Optimizing the grayscaling of projected images and the speed profile of the print simultaneously makes the optimization problem nonlinear. Nonlinear optimization can be computationally expensive depending on the size of the desired part. In this chapter, a method for reducing the number of variables for parts with cylindrical symmetry is explored. A significant reduction in the number of optimization variables reduces computational load and allows for optimizing the printing of much larger parts.

5.1 Symmetry Update to the Model

The formulation presented in Chapter 3 has as many variables as the number of source pixels in the desired parts layer images. The bigger the object, the more source pixels there are in the model. This makes it so that parts larger than a certain size take too long for the code to process, or cause Matlab to crash all together, due to computational limitations. A special case that allows for the reduction of the number of variables significantly in parts that have cylindrical symmetry. Such shapes can be broken down into rings instead of voxels, after slicing into layers. This approach requires modifications to the old formulation since the ring to ring irradiance is needed now instead of voxel to voxel.

To help with visualization, how two rings of a part would look is given in Figure 5.1. Each ring has 2 coordinates, radius r and altitude z. A layer of a full circle would produce πr^2 variables with the voxel approach while the ring approach only produces r variables to solve the same problem. In order to calculate the irradiance caused by a single source ring (r_s) on the target ring (r_t), the source ring is divided into small sections ($d\theta$) and integrated to get the irradiance on any point on the target ring.

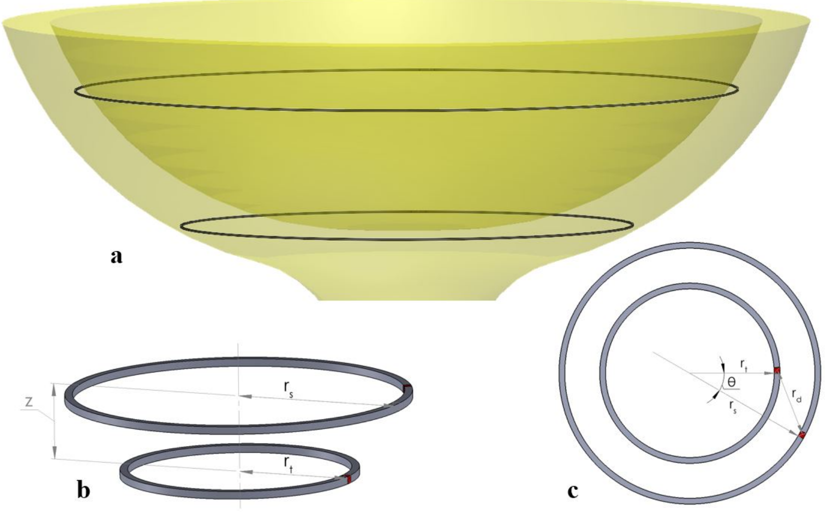

Figure 5.1: (a)An arbitrarily selected set of source and target rings on a goblet CAD. (b)Isometric view of the ring pair with dimensions of the ring section. (c)Top view of the ring pair depicting the parameters used in the formulations.

Irradiance caused by a section of the source ring on the target ring can be written as shown in Eq.(5.1).

$$dI_{single} = a\, e^{-\frac{r_d^2}{2\sigma^2}}\, 10^{-cz}\, dr_s\, r_s\, d\theta \tag{5.1}$$

where $dr_s = 1$. From the cosine law, the distance from the source ring section to the target, r_d, can be written as in Eq.(5.2).

$$r_d = \sqrt{r_t^2 + r_s^2 - 2r_t r_s cos(\theta)} \tag{5.2}$$

Plugging (5.2) into (5.1) and integrating both sides yields

$$I_{single} = a\, r_s\, e^{-\frac{r_t^2+r_s^2}{2\sigma^2}} \int_0^{2\pi} e^{\frac{r_t r_s cos\theta}{\sigma^2}} d\theta\, 10^{-cz} \tag{5.3}$$

$$\int_0^{2\pi} e^{\frac{r_t r_s cos\theta}{\sigma^2}} d\theta = 2\pi J_0\left(\frac{r_t r_s i}{\sigma^2}\right) \tag{5.4}$$

Where J_0 is the Bessel function of the first kind of order zero. Combining (5.3) and (5.4), the irradiance by the source ring on the target can be written as shown in Eq.(5.5).

$$I_{single} = 2\pi r_s\, a\, e^{-\frac{r_t^2+r_s^2}{2\sigma^2}} J_0\left(\frac{r_t r_s i}{\sigma^2}\right) 10^{-cz} \tag{5.5}$$

Energy output onto the target ring by a layer needs to be calculated and then all the layers above the target can be summed to get the total energy absorbed. irradiance from the entire n^{th} layer on the ring at (r_t, k) can be given as

$$I_{layer(r_t,k,n)} = \sum_{r_s=1}^{R_s} 2\pi r_s\, a_{(r_s,n)}\, e^{-\frac{r_t^2+r_s^2}{2\sigma^2}} J_0\left(\frac{r_t r_s i}{\sigma^2}\right) 10^{-c(n-k)} \tag{5.6}$$

where k and n are the vertical coordinates of the target and source rings respectively. Energy deposited by this layer on the target disk is then the irradiance in (5.6) multiplied by the time the image of this layer is projected onto the resin:

$$E_{layer(r_t,k,n)} = t_n \sum_{r_s=1}^{R_s} 2\pi r_s\, a_{(r_s,n)}\, e^{-\frac{r_t^2+r_s^2}{2\sigma^2}} J_0\left(\frac{r_t r_s i}{\sigma^2}\right) 10^{-c(n-k)} \tag{5.7}$$

Combining the energy from all the layers projected before the target gives

$$E_{(r_t,k)} = \sum_{n=k}^{N} t_n \sum_{r_s=1}^{R_s} 2\pi r_s\, a_{(r_s,n)}\, e^{-\frac{r_t^2+r_s^2}{2\sigma^2}} J_0\left(\frac{r_t r_s i}{\sigma^2}\right) 10^{-c(n-k)} \tag{5.8}$$

This formulation allows for the optimization to be performed with far fewer variables and thus with much less computational load, as long as they are cylindrical symmetric.

5.2 Model Based Optimization with Cylindrical Symmetry

After updating the solidification model, the next step is configuring the optimization to utilize the model in order to optimize the grayscaling of images and the time spent on each layer simultaneously to achieve the best possible print quality.

Eq. (5.8) can be rewritten in the form given in (5.9) by collecting many of the terms under w, defined as the irradiance model coefficient.

$$E_{(r_t,k)} = \sum_{nr_s} t_n \cdot a_{(r_s,n)} \cdot w_{(r_s,n,r_t,k)} \tag{5.9}$$

The design variables for this optimization are the grayscale factor $a_{(r_s,n)}$ of each source pixel and the time spent spanning each layer, t_n. All of these variables were collected in the variable vector $\boldsymbol{x}$. The objective function, $J(\boldsymbol{x})$, of the optimization is the sum of energy absorbed by all boundary rings and is given in Eq. (5.10). Boundary rings are rings adjacent to target rings that need to remain uncured.

$$J(\boldsymbol{x}) = \sum_{d=1}^{D} E_d(\boldsymbol{x}) \tag{5.10}$$

where D is the total number of boundary rings and E_d is the energy absorbed by a boundary ring.

The nonlinear optimization problem can be formulated as shown in Eq. (5.11).

$$\min_{x} J(\boldsymbol{x}) \text{ such that } \begin{cases} c(\boldsymbol{x}) \leq 0 \\ \boldsymbol{A} \cdot \boldsymbol{x} \leq \boldsymbol{b} \\ \boldsymbol{lb} \leq \boldsymbol{x} \leq \boldsymbol{ub} \end{cases} \tag{5.11}$$

where the function $c(\boldsymbol{x})$ houses the nonlinear constraints while the matrix $\boldsymbol{A}$ and vector $\boldsymbol{b}$ depict the linear constraints of the system. $\boldsymbol{lb}$ and $\boldsymbol{ub}$ are the lower and upper bound of values elements of $\boldsymbol{x}$ can have. The nonlinear constraints come from the rule that every target ring needs to be cured. To be cured, the energy absorbed by a unit volume on the target ring has to satisfy the inequality in Eq. (5.12).

$$E_{(r_t,k)} \geq E_c \tag{5.12}$$

where E_c is the critical energy of the resin. Every target ring has to accumulate enough energy to be cured, producing one inequality per target ring. $c(\boldsymbol{x})$ is a collection of functions, where the functions are the energy inequalities of each target ring. As an example, function form of the target ring (r_t, k) inequality is shown in Eq. (5.13).

$$\begin{split} c_{(r_t,k)} = -[t_k a_{(1,k)} w_{(1,k,r_t,k)} + t_k a_{(2,k)} w_{(2,k,r_t,k)} + \cdots + t_{k+1} a_{(1,k+1)} w_{(1,k+1,r_t,k)} \\ + \cdots + t_n a_{(R_s,n)} w_{(R_s,n,r_t,k)} - E_c] \end{split} \tag{5.13}$$

The linear constraints of this system come from the acceleration limit imposed on the platform movement. Exerting sudden forces on the part as it is curing can cause defects and sudden changes in the speed of the platform can cause such forces. Therefore an acceleration limit has been introduced in to form of a limitation on the time difference between consecutive layers. The difference in time spent on consecutive layers is limited to 5% of the time spent on a layer without optimization. One such constraint is given in Eq. (5.14).

$$\begin{aligned} |t_n - t_{n+1}| &\leq \frac{t_0}{20} \\ t_n - t_{n+1} &\leq \frac{t_0}{20} \\ t_{n+1} - t_n &\leq \frac{t_0}{20} \end{aligned} \tag{5.14}$$

A total of $(2n - 1)$ linear inequalities are represented in the matrix notation $\boldsymbol{A} \cdot \boldsymbol{x} \leq \boldsymbol{b}$. Once the optimization problem is formulated as shown in Eq. (5.11), the optimization toolbox of Matlab can be utilized to solve the described nonlinear system.

5.3 Validation of the Updated Optimization Method

To test how the optimization can improve a part in real-life printing scenarios, a goblet was modeled and printed. The goblet shape was chosen due to having overhanging structures along with cylindrical symmetry. Having overhanging structures make printing defects easier to recognize in post-print examination of the part. Side view of the goblet CAD is shown in Figure 5.2

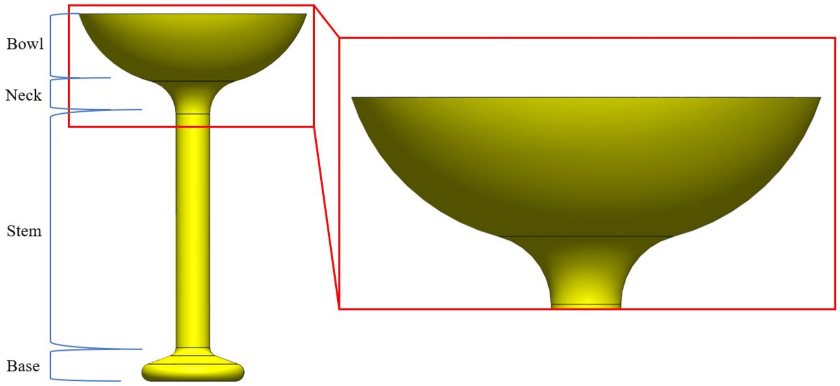

Figure 5.2: Side view of the goblet CAD drawing to be printed. Bowl rim diameter is $5369\mu m$, bowl radius of curvature is $2400\mu m$ and neck radius of curvature is $800\mu m$.

The optimization is focused on the top section of the goblet. For each print, the measured properties are the radii of curvature of the bowl and neck sections, along with the diameter of the top rim. This set of measurements provides a solid framework to judge the dimensional accuracy of a printed part.

In order to put the scale of the parts into perspective, an image of the goblet parts printed with and without optimization on top of a ruler has been provided in Figure 5.3.

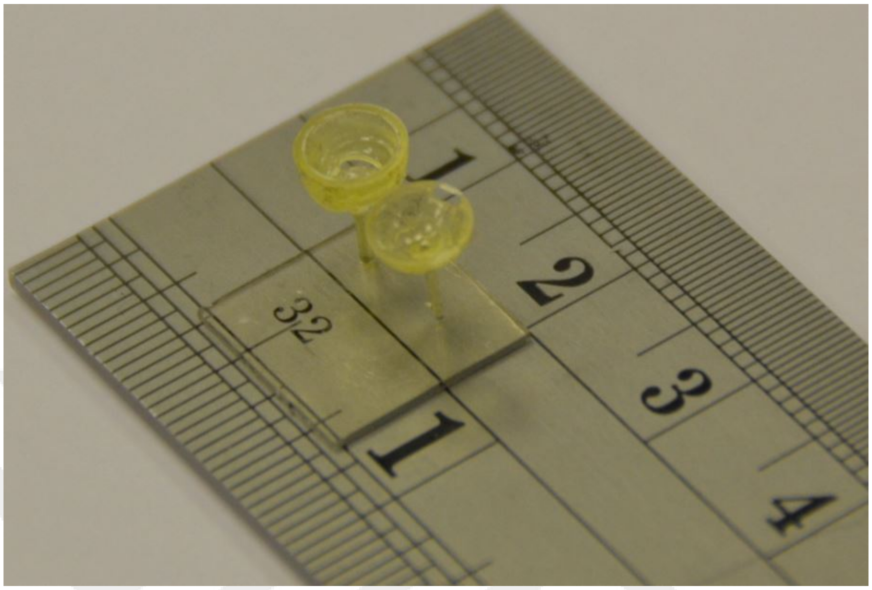

Figure 5.3: Goblet parts printed with(right) and without(left) optimization, on top of a ruler

How the part will look after print with and without optimization is simulated using the model developed in the previous chapters. The results of this simulation are given in Figure 5.4. Figure 5.4(a) is the initial CAD drawing, Figure 5.4(b) is the print estimate without optimization and Figure 5.4(c) is the print estimate after optimization.

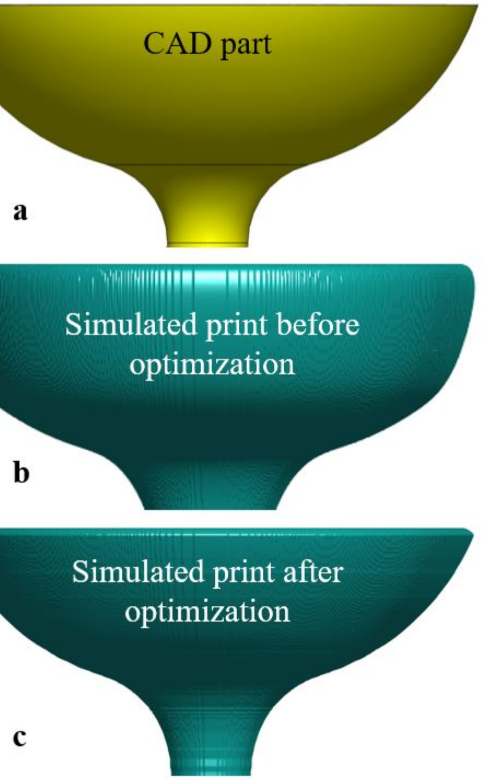

Figure 5.4: (a)Side view of the goblet CAD drawing. (b)Side view of the goblet print simulation without optimization. (c)Side view of the goblet print simulation with optimization.

Figure 5.4(b) shows that overcuring under the bowl along with an overall thicker neck is expected if no changes are made to the layer images or the print speed. Figure 5.4(c) suggests the optimization process will reduce overcuring significantly and produce a part with dimensions much closer to the intended part. In order to achieve this improvement, all layer images have been modified using grayscaling and a new print speed profile has been generated by the optimization algorithm. Figure 5.5 depicts how the speed profile has been altered with respect to time. Before and after of two-layer images are given in Figure 5.6. The first layer shown is from the bowl section and the second one is from the neck section.

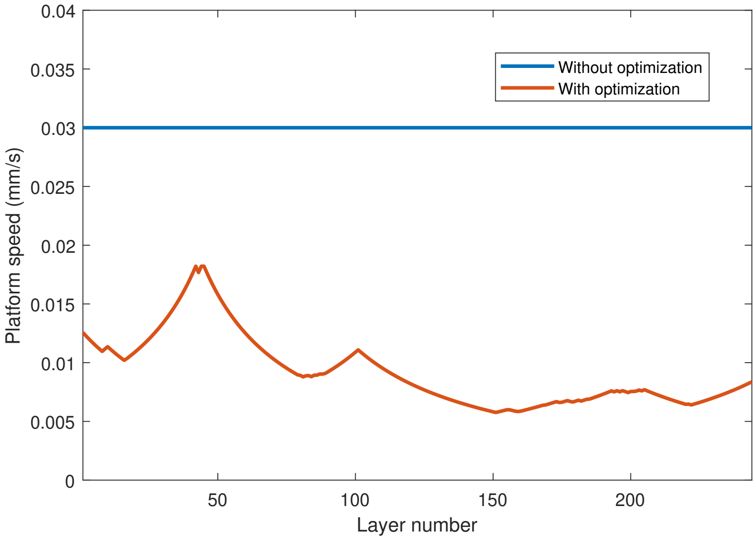

Figure 5.5: Speed profiles of the platform. The blue profile is the base speed without optimization and the orange is the speed profile determined by the optimization.

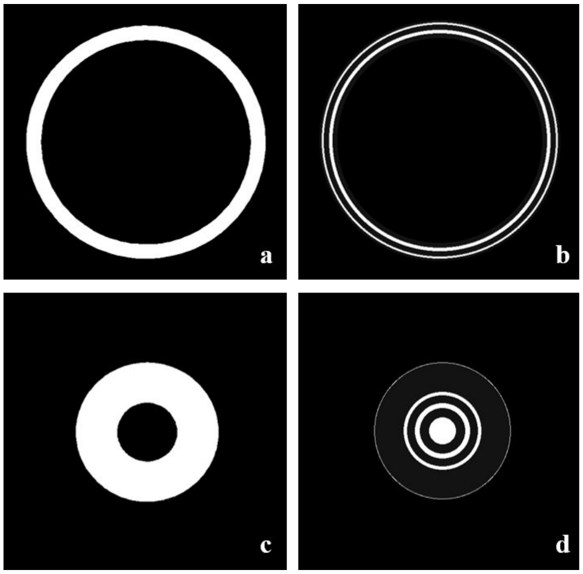

Figure 5.6: Projected images of a layer from the bowl section before(a) and after(b) optimization. Projected images of a layer from the neck section before(c) and after(d) optimization.

Figure 5.5 shows how the new speed profile looks compared to the constant platform speed before optimization. Interestingly the print speed has been reduced even though the model predicts severe overcuring with the initial conditions. A reduction in speed alone increases overcuring however, the algorithm favors a lower print speed along with less light from the projector for more accurate print results. The difference in the amount of light from the projector can be observed by looking at the before and after images of the layers in Figure 5.6. The alterations in the second layer (Figure 5.6(c) and Figure 5.6(d)) are especially interesting. The center section that is meant to remain uncured is lit after the optimization. The cumulative energy deposited on the center of this layer is not enough to cure the resin, Therefore the center section of this image can be lit to provide energy to help cure the lower areas. The target areas of the layer not being lit means that the energy required to cure those regions is provided by the layers projected after this one.

The goblet was printed with and without optimization to validate the improvement promised in the simulation. Images of these printed parts are given in Figure 5.7 and Figure 5.8.

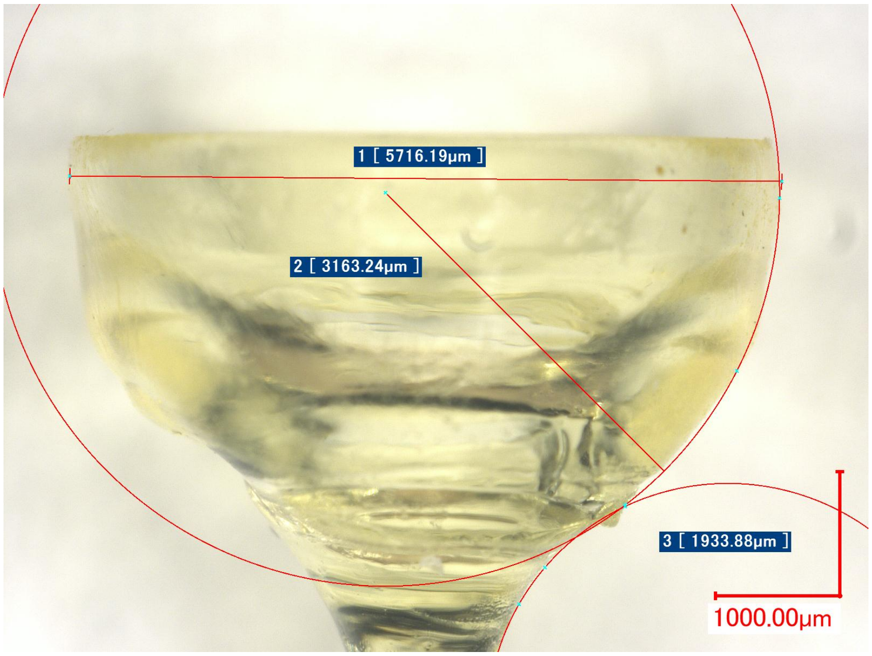

Figure 5.7: Side view of the unoptimized goblet print.

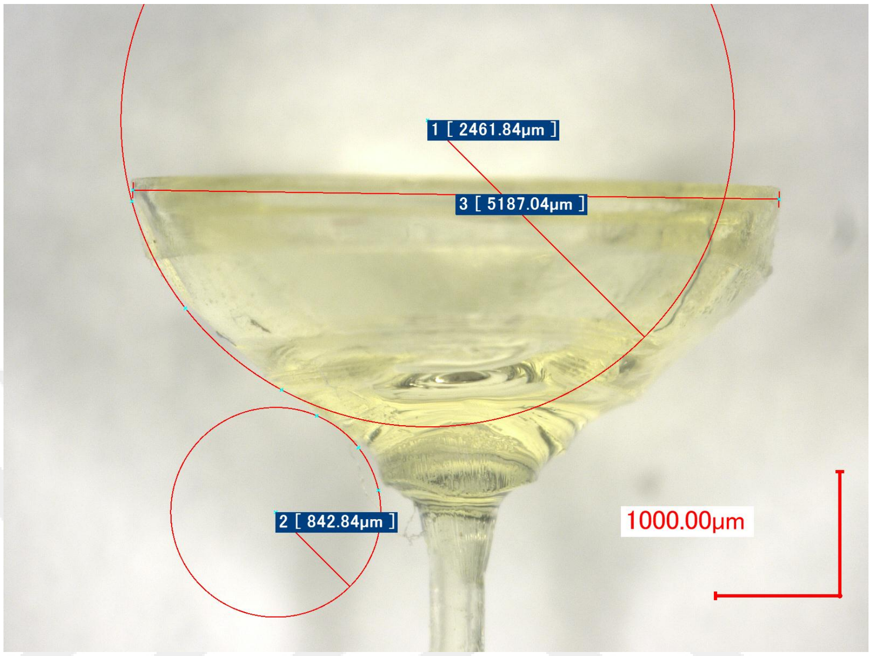

Figure 5.8: Side view of the optimized goblet print.

As seen in Figure 5.7, without the optimization the overhanging areas of the part are significantly overcured and the part is overall thicker, resulting in inflated values in all our measurements compared to the target values shown in Figure 5.2. The optimization fixed the overcuring and produced a part much closer to the desired shape as seen in Figure 5.8. Both the bowl and neck radii of curvature are within 10 of the target dimensions. The stem is thinner than the target part in Figure 5.8 because the print speed at the stem was increased above what the optimization determined. This was done to speed up the print of the irrelevant sections and increase the frequency of part production.

Multiple parts were printed both with and without optimization and their relevant dimensions were recorded. Rim diameter, bowl radius of curvature and neck radius of curvature measurements are presented in Figure 5.9, Figure 5.10 and Figure 5.11 respectively. In all figures the blue line depicts the target value, orange line is the measurement average and the black dots are the individual measurements.

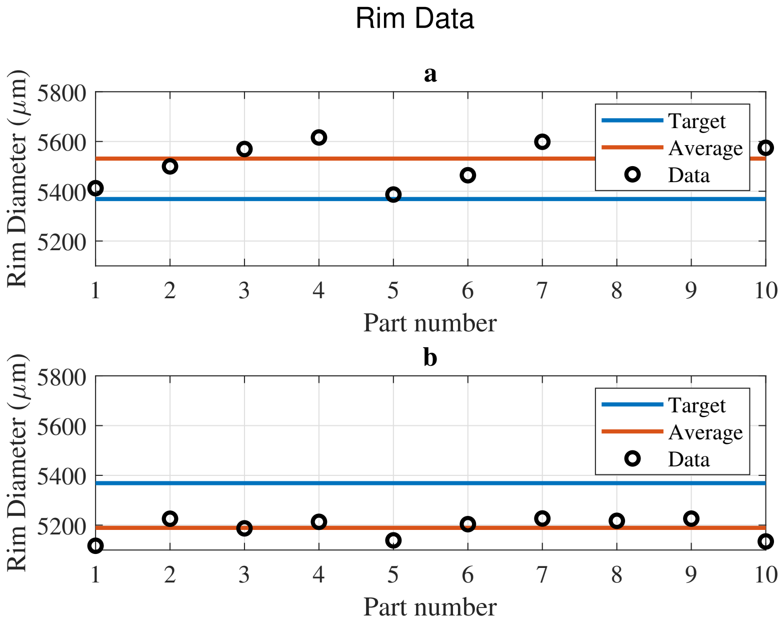

Figure 5.9: Rim diameter data collected from 10 printed parts, (a) before and (b) after optimization

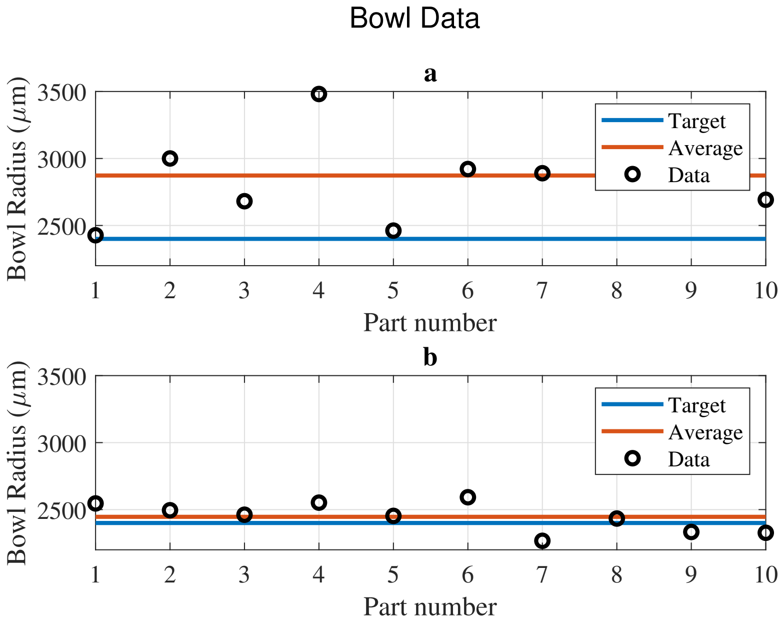

Figure 5.10: Bowl radius of curvature data collected from 10 printed parts, (a) before and (b) after optimization

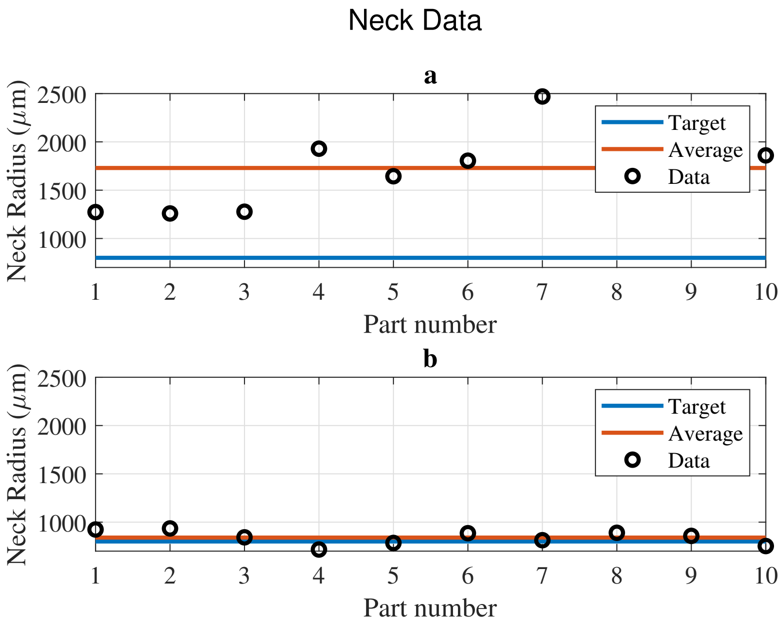

Figure 5.11: Neck radius of curvature data collected from 10 printed parts, (a) before and (b) after optimization

Figure 5.9, Figure 5.10 and Figure 5.11 indicate that the optimization improved the accuracy of the radii of curvature of the bowl and neck sections significantly, while such an improvement is absent from the rim dimensions of the parts. The rim is undercured instead of overcured after the optimization and this occurrence can be explained by examining how the optimization is formulated in 3D. While the optimization is free to control the grayscale value of all the rings on a layer and is not restricted to target rings, it is restricted to layers that include target rings. This means that the optimization cannot add additional rings to compensate for the energy deficit on the topmost layers and those layers exhibit undercuring. Adding blank decoy layers on top for the optimization to alter can solve this issue.

The precision of the printed parts has improved significantly as well, with much lower variance between measurements. Target dimensions for the measured sections are given along with measurement averages with and without optimization in Table 5.1. The standard deviation for all data sets has also been provided.

	Target	**Without Opt. Avg.**	**Std. Dev.**	**With Opt. Avg.**	**Std. Dev.**
Rim Diameter	5369 μm	5531 μm	101.7	5189 μm	42.7
Bowl Radius	2400 μm	2873 μm	321.4	2446 μm	107.7
Neck Radius	800 μm	1730 μm	381.1	840 μm	72.7

Table 5.1 Target value, measurement averages and standard deviations of measurements for the inspected geometries of the part. The inspected geometries for a printed part are the diameter of the top rim, the radius of curvature of the bowl section and the radius of curvature of the neck section.

Chapter 6

Conclusion and Future Work

The work presented in this Thesis documents the development of a model-based dynamic optimization scheme for improving the dimensional accuracy of micro 3D parts produced with vat photolithography.

A projection-based top-down continuous printing approach has been utilized with an experimental setup consisting mainly of a platform attached to a positioning system, a visible light DLP projector, photosensitive polymer resin and a computer that controls the positioning system and the projector. Accurate control of the platform position and the video sent to the projector allowed for not only continuous printing but also variable platform speed during the print.

The Uniz zSG Amber was chosen among others due to it having relatively higher absorption around the wavelength emitted by the projectors blue LED, $444 - 465nm$. While working away from the ideal wavelength range of the resins caused the prints to be slower than what they could have been theoretically, It allowed for finer control over the light absorbed by individual voxels and rings since the prints could be performed slower, disturbing the resin less from platform movement.

The irradiance of light inside the resin was modeled by combining a Gaussian distribution on the horizontal plane with the Beer-Lambert Law. This methodology provided a flexible foundation for developing a very accurate model by calibrating the parameters through experimentation. The model parameters can be determined by examining cured parts alone, however the resin used being transparent made it possible to record how light penetrates the resin, adding another authentication factor for the accuracy of the parameter calibration.

Using Beer-Lambert Law in this way assumes that the resin has the same absorption properties in both solid and liquid form, which is not the case if a resin exhibits photobleaching. Absorption of the resin used in this research was measured in both liquid and solid form and displayed minor photobleaching in the relevant wavelength range. Because the photobleaching is minor, it can be assumed that the integration of the dot test into parameter calibration counteracts the effects of photobleaching.

A segmentation method was introduced as a means of optimizing larger parts that would otherwise be to computationally expensive to optimize. The error caused by this segmentation was reduced by overlapping the sections with each other so that every vowel was part of at least 2 segments. This segmentation method proved useful when optimizing the DNA part and did not introduce a significant error into the system.

Irradiation of light from layer image pixels is mathematically modeled and used to estimate which areas of a 3D part would be cured during a VPP process. Using this model, the layer images are optimized with grayscaling to produce the closest possible print result to the initial CAD drawing of the part. As a result of this optimization, the simulation result is that the number of overcured voxels was reduced by 24.7%. Multiple built parts with and without optimization show that the average notch thickness of the DNA section without optimization is $587 \mu m$ while with optimization, it drops to $476 \mu m$, a value much closer to the desired $479 \mu m$. The optimization also reduced the standard deviation significantly, resulting in a printing method that is both more accurate and more precise.

Micro-scale parts are very prone to overcuring around and under overhanging features. The proposed method allows precise dimensional tuning for micro-scale parts through independent grayscaling of each pixel. Energy absorbed by every pixel is closely regulated to prevent excess light exposure during the print.

The print quality was further improved by allowing the optimization algorithm to vary and optimize the platform speed throughout the print. Simultaneous grayscale and speed optimization is computationally very expensive however, due to the problem becoming nonlinear. Parts with cylindrical symmetry needed to be considered for this approach since their symmetry can be utilized to decrease the number of variable significantly. Utilization of this symmetry allowed for the variable speed optimization to be performed on the goblet part and its dimensional accuracy improved greatly.

The success of this micro vat photopolymerization based approach can also be utilized in larger-scale objects, or parts that do not necessarily have certain symmetries, if certain computational limitations are overcome. Future work includes improving the efficiency of modeling and optimization calculations. One way of achieving this can be reformulating the optimization algorithm such that the constraints are integrated into the objective function and there are no constraints. This would increase the optimization speed and maximum part size since having many constraints slow down the optimization functions.

The current form of the optimization only considers the pixels or ring that appear lit in the layer images to be sources, and this is causing the top of the parts to be subject to undercuring after optimization. This can be overcome by adding additional sources that are not meant to be cured and would only function as extra sources of light to provide the extra light necessary to cure the relevant adjacent areas.

Bibliography

[1] F. Zhang, L. Zhu, Z. Li, S. Wang, J. Shi, W. Tang, N. Li, and J. Yang, "The recent development of vat photopolymerization: A review," *Additive Manufacturing*, vol. 48, p. 102423, 2021.

[2] W. Gao, Y. Zhang, D. Ramanujan, K. Ramani, Y. Chen, C. B. Williams, C. C. Wang, Y. C. Shin, S. Zhang, and P. D. Zavattieri, "The status, challenges, and future of additive manufacturing in engineering," *Computer-Aided Design*, vol. 69, pp. 65–89, 2015.

[3] E. MacDonald and R. Wicker, "Multiprocess 3d printing for increasing component functionality," *Science*, vol. 353, no. 6307, p. aaf2093, 2016.

[4] M. Vaezi, H. Seitz, and S. Yang, "A review on 3D micro-additive manufacturing technologies," *The International Journal of Advanced Manufacturing Technology*, 2013.

[5] P. F. Jacobs, "Fundamentals of Stereolithography," in *1992 Int. Solid Free. Fabr. Symp.*, no. July, pp. 196–211, 1992.

[6] A. S. Limaye, *Design and Analysis of a Mask projection Micro Stereolithography System.* PhD thesis, Georgia Institute of Technology, 2004.

[7] D. Lee, T. Miyoshi, Y. Takaya, and T. Ha, "3D Microfabrication of Photosensitive Resin Reinforced with Ceramic Nanoparticles Using LCD Microstereolithography," *Journal of Laser Micro/Nanoengineering*, 2006.

[8] I. B. Park, Y. M. Ha, and S. H. Lee, “Dithering method for improving the surface quality of a microstructure in projection microstereolithography,” *International Journal of Advanced Manufacturing*, 2011.

[9] K. Mostafa, A. Qureshi, and C. Montemagno, “Tolerance Control Using Subvoxel Gray-Scale DLP 3D Printing,” 2017.

[10] C. Zhou, Y. Chen, and R. A. Waltz, “Optimized Mask Image Projection for Solid Freeform Fabrication,” *Journal of Manufacturing Science and Engineering*, 2009.

[11] C. Zhou and Y. Chen, “Additive manufacturing based on optimized mask video projection for improved accuracy and resolution,” *Journal of Manufacturing Processes*, 2009.

[12] Z. D. Pritchard, M. P. Beer, R. J. Whelan, T. F. Scott, and M. A. Burns, “Modeling and Correcting Cure-Through in Continuous Stereolithographic 3D Printing,” *Adv. Mater. Technol.*, vol. 4, p. 1900700, dec 2019.

[13] J. Bonada, A. Muguruza, X. Fernández-Francos, and X. Ramis, “Optimisation procedure for additive manufacturing processes based on mask image projection to improve Z accuracy and resolution,” *Journal of Manufacturing Processes*, 2018.

[14] Y. Wang, D. Xue, and D. Mei, “Projection-Based Continuous 3D Printing Process With the Grayscale Display Method,” *J. Manuf. Sci. Eng.*, vol. 142, feb 2020.

[15] K. M. Lichade, E. B. Joyee, and Y. Pan, “Gradient light video projection-based stereolithography for continuous production of solid objects,” *Journal of Manufacturing Processes*, 2021.

[16] S. You, J. Guan, J. Alido, H. H. Hwang, R. Yu, L. Kwe, H. Su, and S. Chen, “Mitigating Scattering Effects in Light-Based Three-Dimensional Printing Using Machine Learning,” *Journal of Manufacturing Science and Engineering*, 2020.

[17] K. S. Bhole and B. Kale, “Techniques to minimise stair-stepping effect in micro-stereolithography process: A review,” *Advances in Materials and Processing Technologies*, 2021.

[18] Y. Xu, F. Qi, H. Mao, S. Li, Y. Zhu, J. Gong, L. Wang, N. Malmstadt, and Y. Chen, “In-situ transfer vat photopolymerization for transparent microfluidic device fabrication,” *Nature Communications*, 2022.

[19] H. He, Y. Yang, and Y. Pan, “Machine learning for continuous liquid interface production: Printing speed modelling,” *Journal of Manufacturing Systems*, vol. 50, pp. 236–246, 2019.

[20] K. G. Mostafa, M. Arshad, A. Ullah, D. S. Nobes, and A. J. Qureshi, “Concurrent modelling and experimental investigation of material properties and geometries produced by projection microstereolithography,” *Polymers*, 2020.

[21] M. M. Emami and D. W. Rosen, “An Improved Vat Photopolymerization Cure Model Demonstrates Photobleaching Effects,” *2018 International Solid Freeform Fabrication Symposium*, 2018.

[22] M. M. Emami, M. Jamshidian, and D. W. Rosen, “Multiphysics Modeling and Experiments of Grayscale Photopolymerization With Application to Microlens Fabrication,” *Journal of Manufacturing Science and Engineering*, 2021.

[23] M. M. Emami and D. W. Rosen, “Modeling of light field effect in deep vat polymerization for grayscale lithography application,” *Additive Manufacturing*, 2020.

[24] A. Limaye and D. Rosen, “Process planning method for mask projection micro-stereolithography,” *Rapid Prototyping Journal*, 2007.

[25] Y. Li, Q. Mao, J. Yin, Y. Wang, J. Fu, and Y. Huang, “Theoretical prediction and experimental validation of the digital light processing (DLP) working curve for photocurable materials,” *Additive Manufacturing*, 2020.

[26] S. Westbeek, J. Remmers, J. van Dommelen, H. Maalderink, and M. Geers, "Prediction of the deformed geometry of vat photo-polymerized components using a multi-physical modeling framework," *Additive Manufacturing*, vol. 40, p. 101922, 2021.

[27] Z. Ali, E. Tureyen, Y. Karpat, and M. Cakmakci, "Fabrication of Polymer Micro Needles for Transdermal Drug Delivery System Using DLP Based Projection Stereo-lithography," *Procedia CIRP*, 2016.

[28] Y. Li, Q. Mao, X. Li, J. Yin, Y. Wang, J. Fu, and Y. Huang, "High-fidelity and high-efficiency additive manufacturing using tunable pre-curing digital light processing," *Additive Manufacturing*, 2019.

[29] R. Wicker, F. Medina, and C. Elkins, "Multiple Material Micro-Fabrication: Extending Stereolithography to Tissue Engineering and Other Novel Applications," *2004 International Solid Freeform Fabrication Symposium*, 2004.

[30] E. Tureyen, Y. Karpat, and M. Cakmakci, "Development of an iterative learning controller for polymer based micro-stereolithography prototyping systems," in *2016 Am. Control Conf.*, vol. 2016-July, pp. 852–857, IEEE, jul 2016.

[31] Y. Pan, X. Zhao, C. Zhou, and Y. Chen, "Smooth surface fabrication in mask projection based stereolithography," *J. Manuf. Process.*, vol. 14, pp. 460–470, oct 2012.

[32] K. A. Smith, S. Habibi, M. P. de Beer, Z. D. Pritchard, and M. A. Burns, "Dual-wavelength volumetric stereolithography of multilevel microfluidic devices," *Biomicrofluidics*, 2022.

[33] A. Danielak, A. Basso, C. Budden, K. Weiss, J. Lopez, G. Anand, M. Artemeva, and D. Pedersen, "Enhanced build plate design for vat photopolymerization additive manufacturing," in *Proceedings of the 37th Annual Meeting of the American Society for Precision Engineering*, American Society for Precision Engineering, 2022. 37th Annual Meeting of the American Society for Precision Engineering ; Conference date: 10-10-2022 Through 14-10-2022.

[34] A. Al Rashid, W. Ahmed, M. Y. Khalid, and M. Koç, “Vat photopolymerization of polymers and polymer composites: Processes and applications,” *Additive Manufacturing*, vol. 47, p. 102279, 2021.

[35] S. Nohut and M. Schwentenwein, “Vat photopolymerization additive manufacturing of functionally graded materials: A review,” *Journal of Manufacturing and Materials Processing*, vol. 6, no. 1, 2022.

[36] A. Andreu, P.-C. Su, J.-H. Kim, C. S. Ng, S. Kim, I. Kim, J. Lee, J. Noh, A. S. Subramanian, and Y.-J. Yoon, “4d printing materials for vat photopolymerization,” *Additive Manufacturing*, vol. 44, p. 102024, 2021.

[37] M. Pagac, J. Hajnys, Q.-P. Ma, L. Jancar, J. Jansa, P. Stefek, and J. Mesicek, “A review of vat photopolymerization technology: Materials, applications, challenges, and future trends of 3d printing,” *Polymers*, vol. 13, no. 4, 2021.

[38] U. Shaukat, E. Rossegger, and S. Schlögl, “A review of multi-material 3d printing of functional materials via vat photopolymerization,” *Polymers*, vol. 14, no. 12, 2022.

[39] W. Zhao, J. Zhang, X. Wang, Y. Xu, N. Ding, and Z. Peng, “Vat Photopolymerization 3D Printing of Advanced Soft Sensors and Actuators: From Architecture to Function,” *Advanced Materials Technologies*, 2021.

[40] Texas Instruments, *DLP4710 0.47 1080p DMD datasheet (Rev. A)*, 11 2021.

[41] A. Zhakeyev, J. Tobin, H. Wang, F. Vilela, and J. Xuan, “Additive manufacturing of photoactive polymers for visible light harvesting,” *Energy Procedia*, 2019.